ECAP-2021

Array Component Optimization and Gamma Hadron Separation for SWGO

Master‘s Thesis in Physics

Presented by
Johann Brand
June 25th, 2021

Erlangen Centre for Astroparticle Physics
Physics Insitute
Friedrich-Alexander-Universität Erlangen-Nürnberg

Supervisor: Prof. Dr. Christopher van Eldik
Second referee: Prof. Dr. Stefan Funk

Abstract

The Southern Wide-field Gamma-ray Observatory (SWGO) will be the next generation of extensive air shower particle detector arrays based on Water Cherenkov detection technique. The first generation of these ground based particle detectors was MILAGRO, which was located in the Jemez Mountains near Los Alamos, New Mexico, at an elevation of about 2650 m. The observatory, consisting of a pond and ground-based photomultiplier tubes (PMTs), was commissioned in 1998 and recorded data until April 2008. In the year 2015, the second generation, named High-Altitude Water Cherenkov Observatory (HAWC), was completed. The detector array located at a plateau in Mexico at an altitude of 4100 m uses densely-spaced steel water tanks to observe particles from air showers. Each tank contains four photomultipliers and the entire detector comprises 300 tanks in total. As a next step, SWGO is planned to be a gamma-ray observatory with close to 100% duty cycle and a field of view of ~ 2 sr. It will not only have a larger detector area than HAWC, but also exceeds its sensitivity significantly. It will be primarily based on water Cherenkov detector units and be able to measure energies of 100s of GeV to 100s of TeV. Several array layouts and detector unit designs are under investigation for SWGO. One of these detector unit designs is the cylindrical double layer water cherenkov detector (DLWCDc). To optimize this tank design, a number of studies on radius, height and color configurations of the inner walls were made in this thesis. Furthermore, built on these studies, a method for γ-hadron separation using the upper and the lower layer of this tank design is developed.

Contents

Acknowledgements

Statement of Authorship

List of Figures

List of Tables

1 Introduction to High Energy Gamma Ray Astronomy

Astrophysically, the universe can be observed by looking at photons and other particles such as neutrinos. The energies of electromagnetic (EM) photons can strongly differ and therefore, the EM spectrum is divided into different fields of study depending on the energy which can be seen in figure 1.1. Beyond this division, distinction of photons can be done by having a glance at the emission processes. They could be either thermal or non-thermal. Thermal emission processes of EM radiation are able to provide energies up to a few hundred of keV. However γ-rays with much higher energies were observed, that could only be produced by non-thermal processes which were dominant at the early stage of the Big Bang. In order to understand the emergence of photons produced by non-thermal processes, further investigations have to be done.

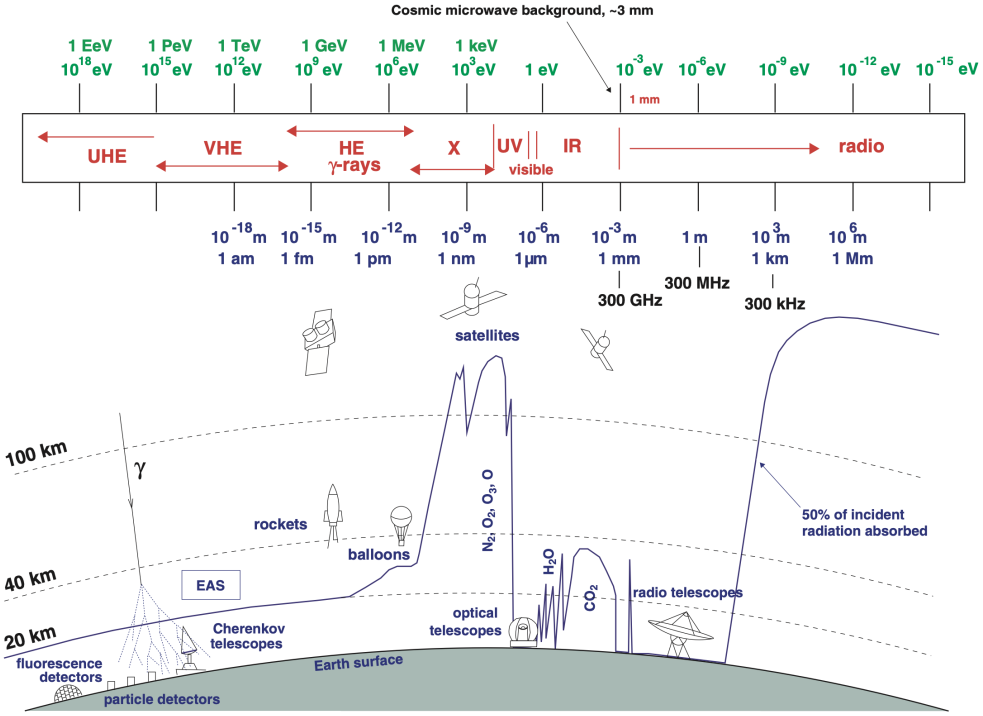

Figure 1.1: The EM spectrum and the different levels of the atmosphere where they become absorbed. The different ranges of EM radiation are labelled in red. (Image from Wagner 2006)

1.1 The Non-Thermal Universe

Hess's discovery of cosmic rays in the year 1912 opened the door to many new discoveries in particle and astroparticle physics (see Blümer et al. 2009). In addition to that, the famous balloon rides brought him the Nobel prize in the year 1936. A conclusion of these rides is that the sources of this ionizing radiation (later referred to as cosmic rays (CRs)) were attributed to be outside the Earth's atmosphere. The study of the non-thermal universe started with this discovery. Nowadays instruments are able to observe CRs with energies up to $\sim 10^{20}$ eV. With these CRs it is possible to study not only non-thermal phenomena which are crucial for the evolution of the universe but also the fundamental physics beyond the energy range which can be reached with man-made accelerators.

Sources of these charged particles are called cosmic accelerators. Pions, positrons and muons were the first particles discovered, later referred to as part of the secondary cosmic rays, which are produced by primary cosmic radiation such as Protons or Alpha-particles (99%). Although CRs are used, in order to obtain information about the composition, energy spectrum and a possible anisotropy for the highest energy ones, their charge poses an issue. Since charged particles are deflected by magnetic fields and since randomly oriented magnetic fields are prevalent in the galactic and inter-galactic medium, the path of the particles cannot be traced. Therefore, their arrival directions cannot be used to point back to their source. In order to study the acceleration sites of these CRs one has to rely on the neutral particles like γ-rays and neutrinos which are a by-products of non-thermal processes and not deflected by magnetic fields.

Since 1936, there have been many new ways to explore these by-products of cosmic rays. In the field of γ-ray astronomy, there are in principle two different approaches for the detection of γ-rays . On the one hand, space based telescopes, e.g. Fermi-LAT, are used, measuring γ-rays by e^-e^+ pair production. On the other hand, ground based telescopes such as the Southern Wide-field Gamma-ray Observatory (SWGO) or the Cherenkov-Telescope-Array (CTA) are utilized to detect γ-rays using the Earth's atmosphere as a first part of the detector. Neutrinos interact with other particles only through weak-interactions with a very small cross-section and are therefore mighty difficult to detect. Nevertheless, noteworthy progresses have been made in the field of neutrino astronomy in the last few years, as well. As γ-ray astronomy is the area of study of this thesis, further in this chapter, CRs and γ-ray astronomy, including a more detailed description of the two detection techniques are described more in detail.

1.2 Cosmic Rays

CRs were discovered by V.F. Hess during several ascends with balloons up to altitudes of 5 km. At these rides he measured the ionization rate of air as function of altitude. There was an increase of ionizing radiation with increasing height detected and he concluded that radiation penetrates from outer space into the atmosphere (Hess 1912). Many more experiments and conclusions on this radiation have been made since his discovery. In the year 1929, W. Bothe and W. Kolhörster measured coincident signals in two Geiger-Müller counters, with placing an absorber material in between the two counters. With this experiment, they concluded that the “Höhenstrahlung” (or cosmic radiation) is of corpuscular nature, i.e. it consists of charged particles (Bothe & Kolhörster 1929). A few years later, in the late 1930s, P. Auger and W. Kolhörster concluded at the same time that the registered particles are secondaries generated in the atmosphere within extensive air showers (EASs), originating from a single primary CR.

1.2.1 Cosmic Ray Flux

The observation of CRs directly or indirectly through extensive air showers (EASs) in several experiments reveals an all-particle spectrum of CRs. Their energies extend from the MeV range to at least 10^{20} eV. The differential energy spectrum falls steeply as function of energy and is depicted in figure 1.2.

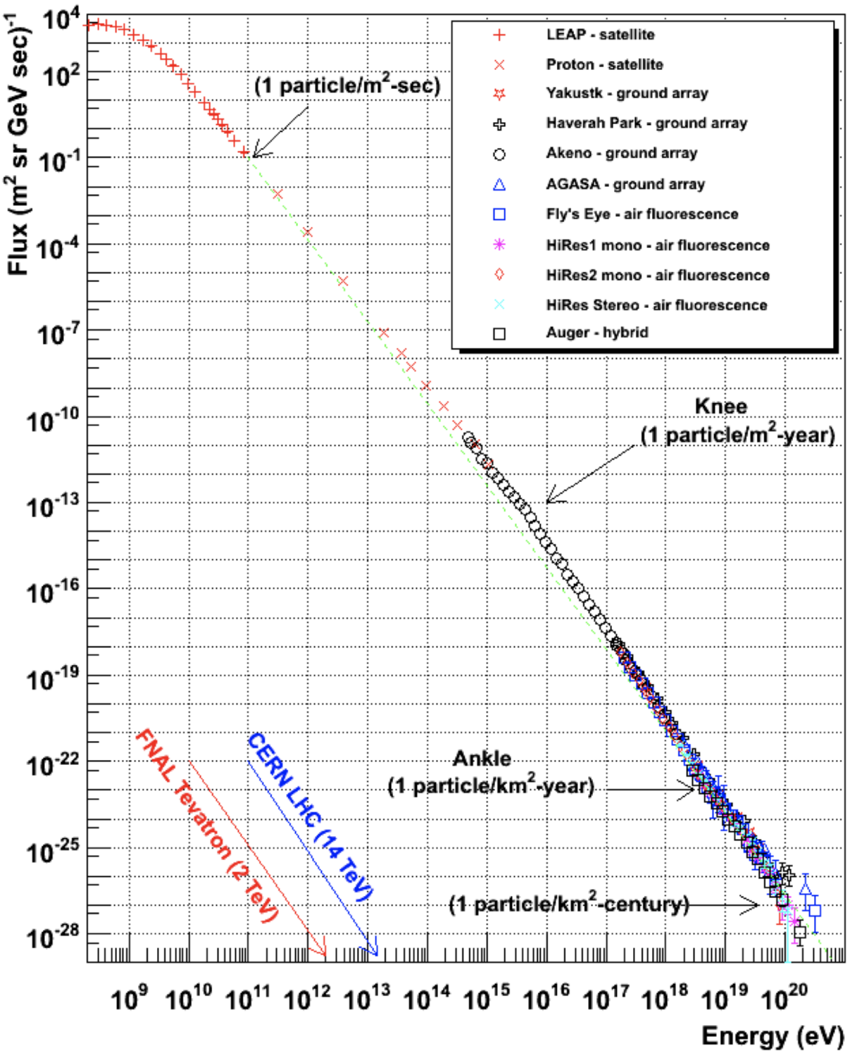

Figure 1.2: Overall energy spectrum of cosmic rays (CRs) from various experiments. Major features as the knee, 2nd knee and the ankle are displayed, as well as the energies that could be provided by the Large Hadron Collider at CERN. (Image from Blandford et al. 2014)

The flux decreases from more than 1000 particles per second and square meter at GeV energies to about one particle per m^2 and year at a PeV and further to less than one particle per km^2 and century above 100 EeV. Particles with an energy beyond 1 GeV, coming from outside of the solar system are blocked by the solar magnetic field. Hence, the lowest energy CRs are most likely generated within the solar system by the solar flares. Above an energy of 1 GeV the spectrum shows several features. The first feature is called the knee of the spectrum that is in the

PeV region. Before the knee, from 100 GeV up to 5 PeV the spectrum follows a power law $\frac{dN}{dE} \sim E^{-\Gamma}$ with spectral index Γ of ∼2.7. In this range CRs are expected to have a galactic origin. For an energy range from 5 PeV up to 0.1 EeV the spectrum follows a power-law with spectral index Γ of ∼3.0. This part of the spectrum is thought to be the interval where the transition from galactic to the extra-galactic origin takes place. From 0.1 EeV up to 5 EeV, which is the position of the 2^{nd} knee, the spectral index changes again to a value of Γ of ∼3.3. This energy range is assosciated with the transition to heavier primaries (Tanabashi et al. 2018). Finally, approximately at 5 EeV the spectrum flattens again at the ankle. After the ankle up to an energy of 40 EeV the index Γ becomes ∼2.6. The origin of these highest energy CRs is most likely to be extra-galactic. At about 40 EeV the spectrum has a hard cut-off. One attempt to explain this is the Greisen-Zatsepin-Kuzmin (GZK) cut-off (Greisen 1966) (Zatsepin & Kuzmin 1966). The GZK cut-off takes the interaction of CRs with the cosmic microwave background (CMB) into account. This limits the maximum distance that can be travelled by CRs of energies 10^{20}eV to at least 50 Mpc. The strong decrease in flux brings up many challenges in detection and also has an influence on our knowledge about the particles and their origin. In the sub-GeV region CRs could be measured with small detectors in outer space. At energies exceeding a few TeV large detection areas are required to collect a suitable number of particles in a reasonable time. Nowadays for this, ground level detectors are realized, where EASs produced in the atmosphere are registered. For more information have a look at section 1.3.2

1.2.2 Fermi Acceleration of Cosmic Rays

In the year 1949 Enrico Fermi proposed an acceleration mechanism, explaining the acceleration of CRs by collision with interstellar clouds. Due to his proposal relativistic particles were reflected and accelerated by this randomly moving clouds, which act like "magnetic mirrors". There is either a gain or a loss in energy depending on its charge whereby the energy gain is more likely than the loss (Fermi 1949). The average energy gain per collision

$$\left\langle \frac{\Delta E}{E} \right\rangle = \frac{8}{3} \left(\frac{v_{\mathrm{cf}}}{v_{\mathrm{p}}} \right)^2 \tag{1}$$

can be described by a power-law, see equation 1 and is proportional to the square of $\frac{v_{\mathrm{cf}}}{v_{\mathrm{p}}}$. Here v_{cf} and v_{p} are the velocity of the cloud and the velocity of the relativistic particle. The name of this process is “Second-order Fermi acceleration” given by the value of the exponent. Even though second-order acceleration succeeds in bringing up a power-law spectrum, it does not convince in every circumstance. Hence, an adequate explanation is needed, which leads to the first order Fermi acceleration also known as the diffusive shock acceleration. The energy gain

$$\left\langle \frac{\Delta E}{E} \right\rangle \propto \left(\frac{v_{\mathrm{cf}}}{v_{\mathrm{p}}} \right) \tag{2}$$

in the first-order Fermi acceleration is proportional to $\frac{v_{\mathrm{cf}}}{v_{\mathrm{p}}}$, in comparison to the second-order acceleration. This leads to a more effective acceleration of relativistic particles in shocks near supernova remnants. If the particle moves with isotropic velocity into a shock it will be diffusely reflected and its velocity will be increased as well. The orientation of the particle's direction is changed from either down- to upstream or up- to downstream. After multiple repetitions of the processes by many particles, the resulting energy gain can be approximated by a power-law:

$$N\left(E\right)dE \sim E^{-2}dE \tag{3}$$

In this case dE is the fractional energy gain and N(E) the number of particles. The power-law index is -2 for the first-order Fermi acceleration as well. For more information see (Bustamante et al. 2010). Summed up it is assumed that particles are diffuse accelerated in shocks which is described by first-order Fermi mechanism. Due to this, the linear energy gain can be approximated for many particles by a power-law with an index of -2. This does not exactly fit to the observed spectral index Γ but is a reasonable approximation for it.

1.3 γ-Ray Astronomy

An introduction into CRs was previously given. In this section the focus is on γ-ray astronomy. As primary CRs are charged particles and due to prevalent magnetic fields in the galactic and extragalactic medium CRs lose their directional information while travelling through space. Meanwhile, however γ-rays are produced by interactions between CRs with the surrounding medium. These γ-rays are neutral and are therefore not deflected by magnetic fields. For this reason γ-rays are excellently suited to study the source environments of the highest energy accelerator sites. As displayed in figure 1.1, the energy spectrum of γ-rays starts with energies of about 1 MeV and really ends with the highest energies above hundreds of PeV. This wide energy range can be spitted up in several sub regions. In this thesis very-high energy (VHE) γ-rays , which have an energy of 50 GeV to 100 TeV are of importance.

1.3.1 Sources of γ-Rays

Presumable sources for high energy cosmic rays and also gamma rays are supernova remnants, surrounding nebular of pulsars, active galactic nuclei (AGN) and gamma ray bursts (GRB's) (see Tinivella 2016). Dark matter annihilation is supposed to be a gamma ray source as well. Supernova remnants considered the major source of galactic cosmic rays. Accelerated particles in supernova remnants are principally protons, He nuclei and e^- from the shocked matter. However, collisions between high energy particles and the supernova remnant matter can result in the production of secondary particles like $p\overline{p}$ and e^-e^+ pairs. The so produced antiparticles are accelerated in the same way as ordinary particles (see Blasi 2009). Now pair annihilation, synchrotron radiation and inverse Compton scattering produce the high-energy gamma rays. An alternative way is that high-energy protons produce photons via π^0 production. The result is a 68 MeV[1] peak in gamma ray spectrum. These ways of producing gamma rays are called the leptonic and hadronic channel. While acceleration in supernova remnant takes place through a shock wave, this occurs in the surrounding nebular of pulsars by rotating magnetic fields of the pulsar.

1.3.2 Detection Techniques

Nowadays there are two main detection techniques in γ-ray astronomy. On the one hand space-based and on the other hand ground-based detection. As displayed in figure 1.1, γ-rays get absorbed in the atmosphere. Therefore the most intuitive way of direct detection is, to put the detector outside of the atmosphere into space. But of course transport into space and hosting in a satellite entail some disadvantages e.g. limitation in size and weight. Especially at high energies, due to the power law behavior of the spectrum with an index around -2.7, the small size comes into effect. The small size and thus the low effective area of about 1 m^2 are only suitable for detection of γ-rays in MeV to GeV energy range. This means for the detection of higher energetic γ-rays , that other methods have to be used. Here ground based detection methods have to be taken into account. Instruments used for this purpose, measure γ-rays indirectly through EASs. Because of this a high effective area can be achieved, allowing a detection of high energetic γ-rays with a low flux. Due to the fact, that this thesis is about SWGO, a ground-based detector, in the following ground-based detection as well as the underlying physics are presented. Indirect methods are used to observe γ-rays with energies above tens of GeV. As mentioned before γ-rays and CRs do not penetrate the atmosphere, but interact with the nuclei that prevalent there. This interaction of a primary particle leads to a cascade of interactions and thus to a so-called extensive air shower (EAS), which can ultimately be used for determination of energy, type and direction of the primary particle (Cui 2009).

1.3.3 Extensive Air Showers

Each time a VHE primary particle enters the Earth's atmosphere an extensive air shower (EAS) is induced. The first interaction normally takes place at an altitude of $10-20$ km above see level. The types of interactions as well as the produced secondary particles within the EAS strongly depend on the type of the primary particle. Whenever the primary is a lepton or a γ-ray , a EM shower is induced. In case of a hadron as the initial particle, the EAS is hadronic in nature. A schematic of a gamma and a hadron induced shower is shown in figure 1.3.

EM Shower

Depending whether the primary particle is a γ-ray or a lepton, which are mostly be electrons, the first interactions will take place at different heights in the atmosphere. From first interaction on, the shower can be separated in stages.

---

[1] half of the π^0 mass

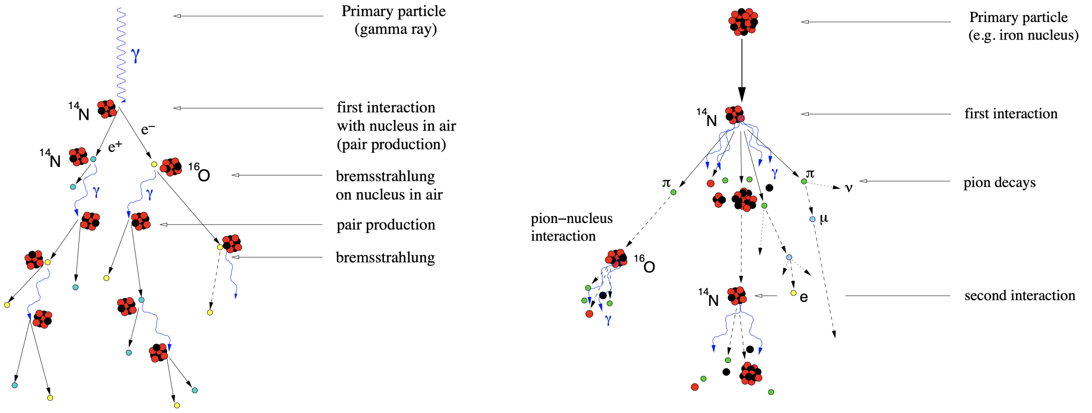

(a) γ-ray induced air showers (b) Hadron induced air shower

Figure 1.3: Schematic of air shower development. A primary particle interacts in presence of a nucleus. (Image from Cui 2009)

The first stage is the initial development stage of the EM air shower, which is dominated by pair-production and Bremsstrahlung. In the later stages the dominant interaction is ionization. A schematic for this is illustrated in the right part of figure 1.3. Bremsstrahlung only takes place for γ-rays with an energy above 1.022 MeV, which is twice the rest mass of an electron. The secondary photons, which can be seen in the figure are produced due to Bremsstrahlung.

Hadronic Shower

Hadronic Showers are dominated by strong interactions. This is the main difference compared to EM showers. In this scenario, the primary particle interacts with the nucleus of the atoms in the Earth's atmosphere. Thereby mesons are created. 90% of these mesons are pions, which decay depending on their charge.

- Charged pions decay into muons and neutrinos:

$$\pi^+ \longrightarrow \mu^+ + \nu_\mu$$
$$\pi^- \longrightarrow \mu^- + \bar{\nu}_\mu$$

  The muons later decay on their own into electrons and neutrinos:

$$\mu^+ \longrightarrow e^+ + \nu_e + \bar{\nu}_\mu$$
$$\mu^- \longrightarrow e^- + \bar{\nu}_e + \nu_\mu$$

- Neutral Pions most likely decay into γ photons:

$$\pi^0 \longrightarrow \gamma + \gamma$$

  The produced γ-rays can start individual sub-showers, which follow the behavior discussed in the previous paragraph about EM showers.

Differences

If one compares EM and hadronic air showers, several differences can be found. These differences will later be used by ground-based detectors for separation between gamma and hadron induced air showers. In the following there is an enumeration of differences.

- EM showers are more compact
- EM showers are more symmetrically distributed around the shower development axis
- Hadronic showers are more dispersed
- Muons produced in hadron induced showers give distinct features

Additional information can be found in (Longair 1992) and (Cui 2009).

1.3.4 Cherenkov Radiation

If a charged particle has a velocity v, which is higher than the speed of light in the medium it is travelling in, it emits Cherenkov radiation. The light is emited in a cone with an aperture angle depending on the velocity of the particle and the refractive index of the surrounding media. The dependency is written down mathematically in equation 4 and can be seen in figure 1.4.

$$cos\left(\theta\right) = \frac{c_{\text{medium}}}{v_{\text{particle}}} = \frac{1}{n\beta} \tag{4}$$

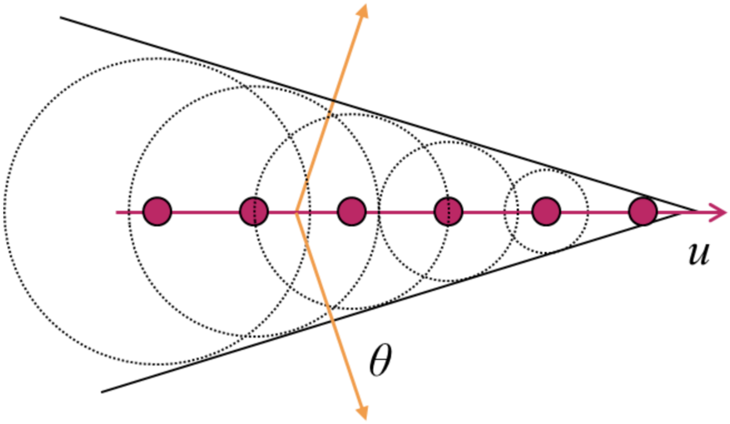

Figure 1.4: Schematic diagram showing the production of Cherenkov light and the geometric expansion due to Huygens construction of the wavefront. Here u represents the velocity of the particle in the surrounding medium, which has to be higher than $\frac{c}{n}$. (Image from Alaeian 2014)

For water, the refractive index $n = 1.33$, leads to an angle θ of 41.2°. The refractive index n of air has a value of 1.0003 and therefore the angle θ is about 1° (HAWC 2011). The threshold energy E_{min} to produce Cherenkov radiation for a particle of mass m_0 can be written as:

$$E_{\text{min}} = \gamma_{\text{min}} m_0 c^2 = \frac{m_0 c^2}{\sqrt{1 - n^{-2}}} \tag{5}$$

Here γ_{min} is the Lorentz factor of the moving charged particle. Because of the direct proportionality of E_{min} and m_0 it can be concluded, that E_{min} is lower for lighter particles, therefore, the Cherenkov radiation production is dominated by them. The spectrum of the Cherenkov radiation has a peak in the range of blue to ultraviolet wavelengths. This peak is clarified by the Frank-Tamm formula (see equation 6), which describes the number of Cherenkov photons produced at a wavelength λ, by an ultra-relativistic particle while travelling a length X in a given dielectric medium.

$$\frac{d^2N}{dx d\lambda} = 2\pi\alpha Z^2 \lambda^{-2} \left(1 - \frac{1}{\beta^2 n^2(\lambda)}\right) \tag{6}$$

In equation 6, shown above, Z is the charge of the particle and $\alpha \approx \frac{1}{137}$ is the fine structure constant. Further information is provided in (Frank & Tamm 1937) and (Longair 1992).

1.4 Ground-Based Experiments

Ground-based gamma-ray astronomy relies on the detection of EASs initiated by the interaction of gamma rays with the Earth's atmosphere. In this section, two types of detection techniques are briefly introduced. In figure 1.5 both are illustrated. On the one hand, IACTs which are pointing instruments with a typical field-of-view of a few degrees and a duty-cycle of 10-20%, on the other hand particle detector arrays, with a very wide field-of-view of about 90° and a duty-cycle of $\sim$ 100% (see Schoorlemmer 2019).

IACTs

While penetrating the Earth's atmosphere, the charged particles of EASs are emitting Cherenkov light. The whole EAS produces a Cherenkov light pool with an aperture of about 1° and a typical radius of 104 m at ground level. Parts of this light pool can be collected by the telescopes, using large mirrors, which focus the light onto a camera. The recorded image of the EAS will be reconstructed later on to estimate the shower properties. For detection of the weak bluish Cherenkov light flashes by IACTs, a huge light detections surface, dark nights and a very short exposure time of the cameras are required (see Durham University 2014). The technique of IACTs was pioneered by the Whipple telescope which detected TeV γ-ray emission from the Crab Nebula in 1989 (Weekes et al. 1989). Further developments were made, which resulted in a second generation of IACTs.

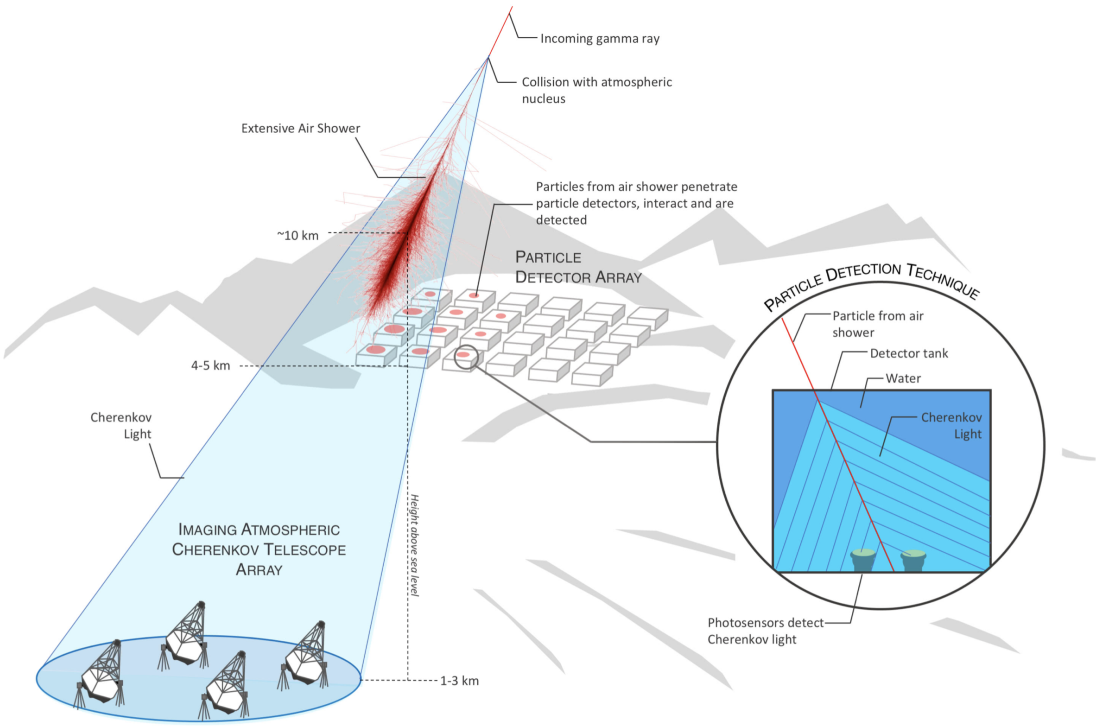

Figure 1.5: Schematic of two complementary detection techniques of high-energy gamma rays. In the left, the imaging atmospheric cherenkov telescope (IACT) technique. Here the Cherenkov light pool produced in the atmosphere by EASs is detected using imaging telescope. In the right, the EASs particle detector array, which detects the secondary particles of EASs directly at high altitudes. (Image from Schoorlemmer 2019)

Examples are the Cherenkov Array at Themis (CAT) (Barrau et al. 1998) and the High Energy Gamma-Ray Astronomy (HEGRA) γ-ray observatory (Aharonian et al. 2000). In the early 2000's, significant improvements came up with High Energy Stereoscopic System (HESS) (Hinton 2004) in the southern hemisphere, Major Atmospheric Gamma Imaging Cherenkov Telescopes (MAGIC) (Fernandez 2006) and Very Energetic Radiation Imaging Telescope Array System (VERITAS) (Holder et al. 2009) in the northern hemisphere as the third generation. These third generation telescopes have lowered the energy threshold to few tens of GeV and improved the flux sensitivity an order of magnitude. They have detected more than 200 galactic and extragalactic sources. An example to show that the development of IACTs is still going on is CTA, which is planned to be an observatory on two sites on Earth. A total of more than one hundred telescopes are planned on both locations, aiming to provide energy coverage for gamma rays from 20 GeV to at least 300 TeV, to give CTA reach to high-redshift and extreme accelerators (see Acharya et al. 2018).

EAS Particle Detector Arrays

This technique relies on the detection of secondary particles of the EASs. Therefore, an array of particle detectors is positioned over a large area. The array has to be set up at high altitudes near to the depth of the shower maximum X_{max}, to be able to detect the secondary particles. The array consists of several units equipped with PMTs. The PMTs detect light either from scintillation or Cherenkov radiation using water cherenkov detectors (WCDs). Time and charge information of the signal observed by the PMTs is utilized for shower reconstruction to gain access to information about the primary particle. One example for a WCDs based EAS particle detector array is HAWC, which is located in the northern hemisphere. It has already shown several exciting results since the full deployment of the observatory in March 2015 (see HAWC 2011). However, such a facility has never been in operation in the southern hemisphere. Access to the Galactic Centre and complementary with the major facility CTA-South are key motivations for SWGO.

Differences between IACTs and EAS Particle Detector Arrays
Both of the above introduced ground-based detection techniques are complement to each other. For an energy range of few tens of GeV to tens of TeV IACTs are the suitable choice. However, for higher energies from a few TeV to few hundreds of TeV EAS Particle Detector Arrays are more appropriate. The angular and energy resolution of IACTs is better compared to that of EAS arrays. On the other side, IACTs are optical instruments and therefore be able to operate in dark nights or moderate moonlight only, while EAS particle detector arrays have no such limitation and have almost a duty cycle of $\sim 100\%$. In conclusion, both techniques are important to observe the different parts of the VHE γ-ray sky. As SWGO takes place a key part in this thesis, it will be introduced more in detail in the following chapter.

2 The SWGO γ-ray Obervatory

The Southern Wide-field Gamma-ray Observatory (SWGO) is planned to be the next generation ground-based water cherenkov detector (WCD) array. Therefore, the SWGO Collaboration was founded in July 2019 by a group of about 40 institutions from 9 countries. The new observatory aims to be the first EAS Particle Detector Array in the southern hemisphere and is benchmarked on current arrays like HAWC in Mexico and the Large High Altitude Air Shower Observatory (LHAASO) in China. The SWGO collaboration plans to explore new layouts and technologies in order to increase the overall sensitivity, as well as the measurable energy range. An other idea is to equip each WCD unit with the capability of tagging muons in order to enhance γ-hadron separation. The core concept for SWGO is described in table 2.1. Due to this, a baseline detector configuration was established, which consists of a high densed core, with an area of about $80,000\ \mathrm{m}^2$ and a high fill-factor above 80% (equivalent to 5x the HAWC main array instrumented area), as well as a larger and spared outer array with an area of $200,000\ \mathrm{m}^2$ and a fill-factor of about 8%. This detector configuration in principle is based on (Schoorlemmer et al. 2017) and (Assis et al. 2018) and is able to provide a low energy detection threshold and good sensitivity to high-energy events at the same time (see Barres de Almeida 2021). A conceptional design with a comparison to HAWC is shown in figure 2.1.

	THE OBSERVATORY CORE CONCEPT
I	High-altitude particle detector above 4.4 km a.s.l
II	Latitude range between 15° and 30° latitude south
III	Wide energy range reaching down to 100 GeV and beyond 100 TeV
IV	High fill-factor core (> 4x HAWC) for significantly better (> 10x) sensitivity, plus large, sparse outer array
V	WCD units with muon counting capability

Table 2.1: Summary of the core concept planned for SWGO. (Table from Barres de Almeida 2021).

There is not only the detector array under investigation, but also various WCD units are currently tested. Possible solutions are based on previous units used in HAWC or LHAASO. Also absolutely new ideas, like the installation directly in a natural lake or pond are taken into account. In summary there are many possible solutions for the array and the WCD units. The choice of course strongly depend on the location and the prevailing conditions and infrastructure of the site. Important for the site choice, are on the one hand the core concepts listed in table 2.1 and on the other hand the average yearly temperature above freezing point, access to water sources, as well as existing infrastructure including roads, power, optical cable, etc.. The total construction cost is estimated to be 54M USD. For all the concepts the budget has to be considered as well as the compatibility with science-driven design goals. Among the possible locations, are the Atacama Large Millimeter/submillimeter Array (ALMA) site in the high plateau of the

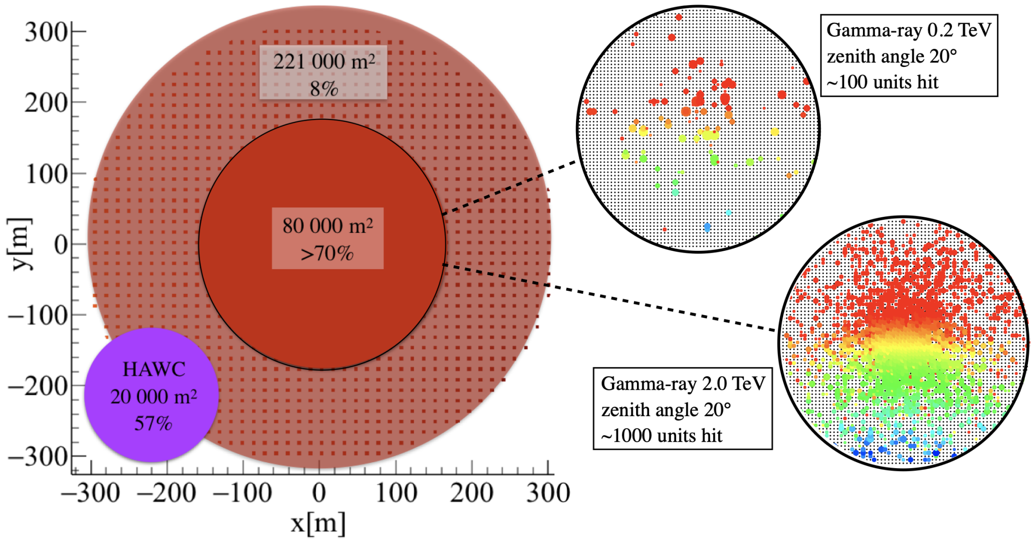

Figure 2.1: A conceptual design of an array at 5 km altitude, with a high fill-factor inner core and a sparse outer array. In the right, the signals of a 200 GeV and 2 TeV gamma-ray simulated showers are shown. The color coding indicates the time gradient of the signals recorded by the detection units. (Image from Schoorlemmer 2019)

Atacama Desert in Chile, the Cerro Vecar in Argentina where QUBIC and LLAMA were built, the ALPACA site in Bolivia and Laguna Sibinacocha, the highest altitude large lake, located in Peru (see Abreu et al. 2019). The goal of the SWGO collaboration is to finalize a design proposal in 2022. In the following a closer look into the DLWCDc as well as the Reference configuration will be taken. Both are part of the simulations and analysis which were carried out in this thesis.

2.1 DLWCDc

A base design of a DLWCDc for SWGO is a cylindrical steel tank. As shown in figure 2.2, the tank is segmented in two layers.

The tank is filled up to the top with water. In both cells of the tank is at least one PMT. In the upper cell the PMTs are facing upwards, while those in the lower layer are installed on the top of the cell, looking downwards. More informations about PMTs is mentioned in section 2.2. As known from section 1.3.3, the secondary particles of an EAS mainly consist of $e^{\pm}$, γ and muons. These particles now enter the WCD and produce Cherenkov light (see section 1.3.4), which will then be detected by the installed PMTs. The water in the WCDs, is perfectly suitable for the Cherenkov light production, due to its high refractive index. The modular structure of the SWGO WCDs makes them optically isolated from each other, which has two benefits. Firstly, it helps to treat them separately during construction or for maintenance. Secondly, it aids to identify the local variations in the observed EASs, providing a strong γ-hadron separation power. The tank dimensions as well as the linings of the inner walls of the tanks haven not been fixed yet and will be under investigation in the analysis part in chapter 3 of this thesis. Nevertheless a short introduction for both is given below.

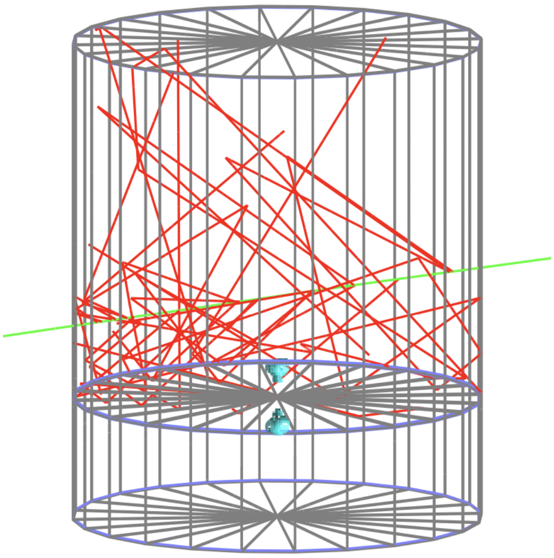

Figure 2.2: Simulation with Geant4 of a DLWCDc unit, crossed by a γ-ray. The green line represents the simulated γ-ray , the red lines optical photons.

Dimensions of the tanks

The height of the upper layer has to be chosen depending on the radius of the tank, so that Cherenkov photons are able to reach any position on the bottom of the upper cell. For simplification, assuming that a vertical particle enters the tank from the center of the roof, the Cherenkov photons should be able to reach the lateral walls of the upper layer. With the information of section 1.3.4 about Cherenkov Radiation, equation 7 can be obtained.

$$h = \frac{r}{tan(\theta_C)} \tag{7}$$

As displayed, the height h of the upper layer depends on the radius r and on the Cherenkov angle θ, which corresponds to 41.2° in water. The lower layer is intended for muon tagging, improving the γ-hadron discrimination. Furthermore it can also be used for reconstruction in case of saturation of the upper layers PMTs. Hence the lower layer height is independent of the radius.

Linings of the inner walls

The inner surface of the tanks is covered with a light-tight liner or bladder. In both layers and for every surface within the tank the liner can be chosen independently of the other liners. In this thesis and also within the reference design and the super configuration (see section 2.3), both reflective (Tyvek) and non-reflective

(Polypropylene) linings are used. The reflectivity of the materials depend on the wavelength of the incident photons. It can take on values between zero and one. A value of one describes a total reflection. Vice versa, if the value is zero, there is no reflection at all. On the one hand polypropylene has a reflectivity of 0.10 in the wavelength range of $275 - 650$ nm. On the other hand Tyvek has a reflectivity of $0.63 - 0.92$ in the range of $250 - 650$ nm. Both reflective (Tyvek) and non-reflective (Polypropylene) materials have different benefits. The reflective linings allow a better detection capability, but might delay the detection time, due to multiple reflections of Cherenkov photons on the walls before they reach the PMTs. Whereas the opposite is true for the non-reflective linings.

2.2 Photomultiplier Tubes

This chapter provides an overview over the most important PMT components and their functionalities, based upon references (Hamamatsu Photonics K.K 2007) and (S.-O. Flyckt, Carole Marmonier 2002) A photomultiplier tube (PMT) converts light into an electrical signal, then amplifies that signal to a useful level by cascade of secondary electrons. They are sensitive to single photons and have a very fast response time of tens of nanoseconds. The work of PMT utilizes the basic principle of the photo-electric effect. Figure 2.3 shows a schematic.

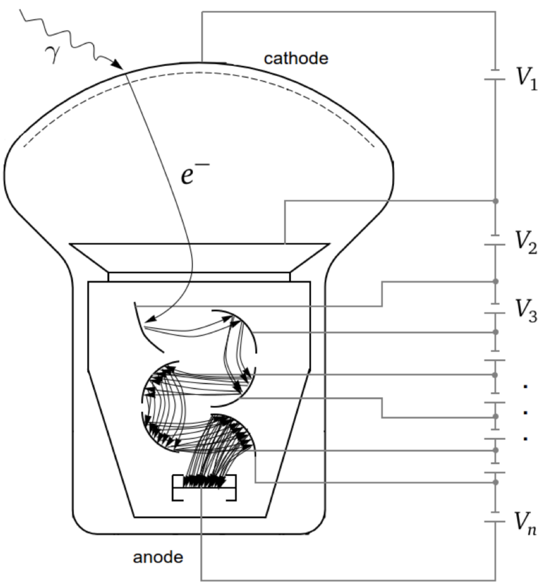

Figure 2.3: Scheme of a photomultiplier tube. The inner structures of the PMT are enlarged and modified in the scheme for better visibility. A primary electron is released from the photocathode (top), is focused to the first dynode by the focusing electrode and produces secondary electrons. Each secondary electron is multiplied due to secondary emission as it travels from dynode to dynode. The secondary electrons then finally reach the anode (bottom), where the electric signal can be measured. (Image from Raffaela Solveig Busse 2017)

In principle PMT consists of the following elements:

- a photocathode which converts light flux into electron flux
- an electron-optical input system which focuses and accelerates the electron flux
- an electron multiplier consisting of a series of secondary-emission electrodes (dynodes)
- an anode which collects the electron flux from the multiplier and supplies the output signal

When a Cherenkov photon hits the photo-cathode of the PMT it can produce a photo-electron (PE) via the photo-electric effect. This ejected PE then accelerates to the first dynode where it ejects more electrons. The number of PEs increases at each dynode. In the end, at the anode, the resulting signal is measured. The probability of a photon entering the photo-cathode and in turn producing a certain signal can be characterized by the quantum efficiency (QE) of the given PMT. The QE depends on many factors like the photo-cathode material, wavelength of the incident light, location of the impinging photon on the photo-cathode and the landing of the PE on the first dynode. In the studies presented later, 8" Hamamatsu R5912 PMTs are used.

2.3 Reference Design

The reference design is part of a bigger array called super configuration. This covers a much larger area and also includes some outrigger clusters of tanks (see Figure 2.4).
Especially the reference design is made for comparison, cost-estimate and generating instrument response functions. It contains 6601 tanks. The array arrangement is shown in figure 2.5. Each tank has a radius of 1.9 m and a a total hight of 3m. The lower layer has a height of 0.5 m and the upper layer has a height of 2.5 m. The lining itself in the reference design is different in the top and the bottom layer and also differs within one cell. In the upper cell the bottom and the top lining is Polypropylene, while the wall lining of the cylinder is made out of Tyvek. The bladder in the lower layer is fully Tyvek. In each layer of the tanks there is one 8” Hamamatsu R5912 PMT. In the upper cell the PMTs are facing upwards, while those being installed in the lower layer on the top of the cell are looking downwards (see Figure 2.2). The DLWCDcs configuration used in the reference design is summarized in table 2.2

2.4 Simulations

In order to investigate the influence of different tank designs and to find a γ-hadron separator, simulations of air showers and detector response are needed. Software required for this is being developed based upon that of HAWC to speed up the process. Even more, this allows a comparison to the performance of HAWC.

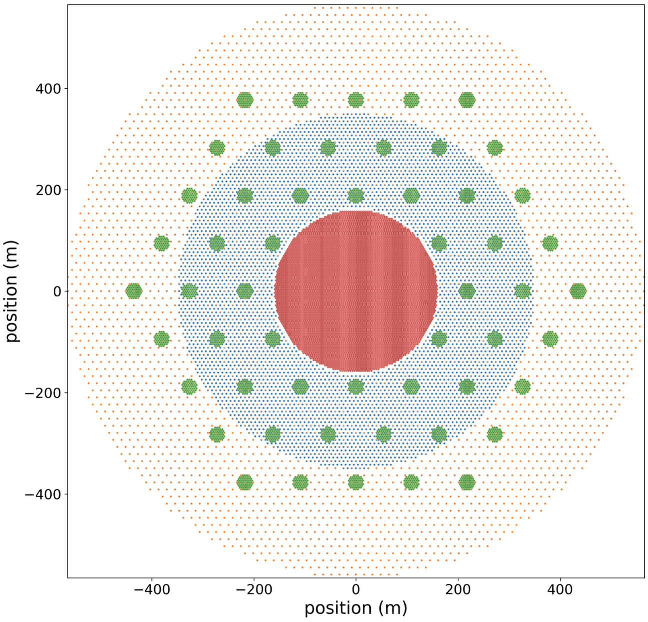

Figure 2.4: Tank positions of the super configuration. The colors indicate different parts of the array.

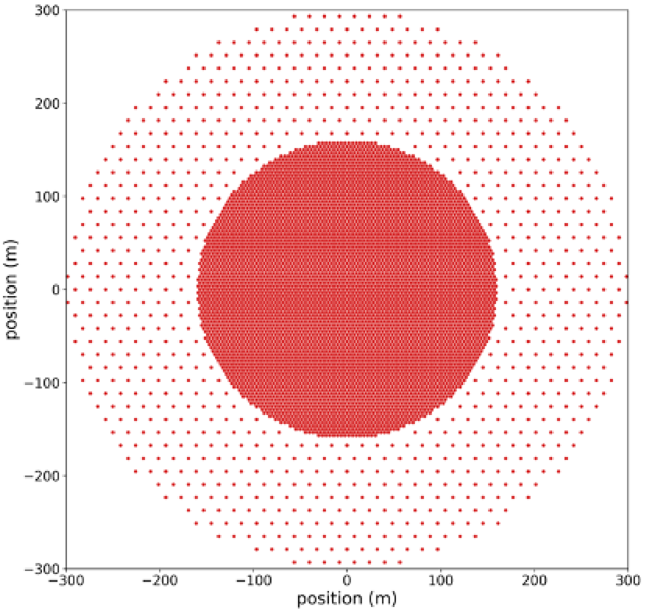

Figure 2.5: Tank positions of the reference design. The inner denser array has a radius of 160 m, the other array a radius of 300 m. The inner array in combination with the outer array includes 6601 tanks.

At the moment the software is usable for the SWGO collaboration only, but in the future it should be available for everyone. The software package **CO**smic **R**ay **SI**mulations for **KA**scade (CORSIKA) (Heck et al. 1998) is used for air showers. This makes it possible to simulate the propagation of primary particles in the atmosphere, obtaining a distribution of secondary particles at a preset

	Upper layer	Lower layer
Wall lining	Tyvek	Tyvek
Cover lining	Polypropylene	Tyvek
Bottom lining	Polypropylene	Tyvek
Height [m]	2.5	0.5
Radius [m]	1.8	1.8
PMT sizes	8”	8”

Table 2.2: Tank configuration of the in the reference design used DLWCDcs

altitude (For this thesis the altitude is set to 4700 m). To simulate the detector responses, a package based on Geant4 (Agostinelli et al. 2003) simulations named HAWCSim is used. HAWCSim picks up CORSIKA’s simulated ground level particles and propagates them through a predefined array of simulated water Cherenkov detectors to produce Cherenkov photons. These Cherenkov photons are then detected by using simulated PMTs. The in this way received data include not only information about the primary particles but also about timing and the number of triggered PE of each tanks PMTs. In this thesis, CORSIKA showers as well as HAWCsim will be used to perform the analysis.

3 Tank Design Optimization

In the previous chapters SWGO and the physics behind were introduced. In this part of the thesis a closer look into the DLWCDcs detector unit design is taken. Therefore the average number of PEs and the single tank trigger probability for different inner wall linings and tank dimensions were under investigation. In the following, first the used CORSIKA air showers and the tank array, as well as the different simulated tank parameters are introduced. After this the results are presented, to motivate a selection of some of the components of the DLWCDcs for SWGO.

3.1 Simulation for the Optimization

In order to perform detailed simulations to study the effect of different DLWCDc properties on the working of the array at first, a set of CORSIKA air showers and a suitable tank array have to be chosen.

3.1.1 Air Shower Simulations

γ-ray induced air showers were simulated using the CORSIKA air shower simulation package, which is widely used and tested in the community. The studies on the tank design optimization were done with a total of $500,000$ simulated CORSIKA showers, thrown exactly at the center fo the detector array. They were distributed over an energy spectrum, following a power law with a spectral index $\Gamma = 2$. The energy spectrum starts at 31.6 GeV and ends at 1 PeV. All showers had a zenith angle of 0° and were observed at an altitude of 4700 m.

3.1.2 Detector Simulations

After the simulation of air showers, the secondary particles of the showers are propagated through the WCDs using HAWCsim, which is described more in detail in chapter 2.4. At this point of the simulation chain, detector characteristics are applied. Therefore various detector components with their properties and different detector layouts were defined. The detector layouts used are summarized in table 3.1. A more detailed description of each component is given on the next page.

Component	Types
Inner wall colors	Black (Polypropylene), White (Tyvek),
Upper cell height	2 m, 3 m, 4 m
Upper cell height	0.75 m
Tank radius	1 m, 2 m, 3 m
PMT sizes	8”
Array layouts	Column and Realistic

Table 3.1: Different DLWCDc layouts used for the tank design optimization.

Inner Wall Colors: As described in Table 3.1, two tank color configurations are simulated that are named black and white. From now on it will only be referred to the wall color inside the tank. This is because we are only interested in the light distribution inside the WCD.

- **Black Tanks:** All the three sections of the tanks cells, which are the bottom lining, wall lining and cover lining are Polypropylene for both the upper and the lower layer. Polypropylene has a defined reflectivity of 10% at a wavelength range from 275 to 650 nm.
- **White Tanks:** In the upper cell only the wall lining is Tyvek and the rest, bottom and cover linings are Polypropylene. In the lower cell all linings are made of Tyvek. Tyvek has a reflectivity of 63% – 92% over the same range on wavelength range from 250 to 650 nm.

Tank Dimensions: When talking about tank dimensions not only physical optimization has to be taken into account, but also costs. Larger tanks bring up higher costs in building the tanks as well as in transportation. Roads and trucks also limit the radius of the tank. Therefore the goal is to find a solution with suitable results, without spending much money per tank. To look at the influence of the tanks height and radius, on for example the average number of PEs, three different upper cell heights and radii, listed in table 3.1 are used. Even though in this thesis the height of the lower layer is kept at a constant level, the signal of the lower cell is analyzed and a dependency on the height of the upper layer can be seen. Beyond the work done here, the lower cells hight can be optimized later on as well.

Layouts: To study the effect of various tank wall colors and tank dimensions on the observed signal, two different layouts named column and realistic layout are used. For both layouts, the description is below:

- **Column Layout:** In Figure 3.1, the schematic of the column layout, for a tank radius of 2 m is shown. This example includes in total 302 DLWCDcs. There is no separation between the two tanks in a column and also the separation between the tanks in one column is 0 m. The layout is parallel to the geomagnetic field at the simulated site. All the showers were thrown exactly at the center of the array with zenith angle 0°. With this layout it is possible to make tank studies up to distances of $\sim$ 300 m. If the radius of the tanks is changed, the number of them within the layout will be increased or decreased. Hence the maximal observation distance is held constant. For a radius of 1 m the number of tanks is 602. When the radius is increased to 3 m the number of tanks within the array is decreased to 402. A column layout is an excellent option for the studies involving the observed signal's amplitude distribution as a function of distance from the center of the shower core. In comparison to the simulation of a more realistic layout, the simulations with the column layout reduce computational power and speed up the analysis.

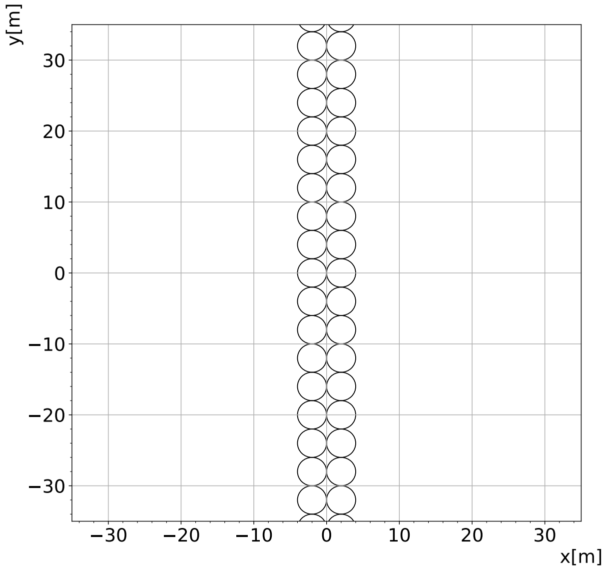

Figure 3.1: A zoom in of the column layout. The circles represent tanks with a radius of 2 m. The whole column layout extends on the y-axis from -300 to 300 m, while the center of the array is at $(0, 0)$. There is no separation between the two tanks in one column, as well as between two columns. The orientation of the layout is parallel to the geomagnetic field.

- **Realistic Layout:** It consists of 6275 tanks, 4872 of them are in the inner part and 1403 are part of the outer array. They are distributed as shown in Figure 3.2. The array is called realistic because it is close to the baseline detector configuration described in chapter 2. It consists of a high dense core, with a high fill-factor of $\sim 80\%$ and a larger and spared outer array with a fill-factor of about 8%. The inner core has a radius of 160 m, while the outer part goes from 160 m up to 300 m from the center of the array. The realistic layout is appropriate to study the number of triggered units. It was used instead of the reference design (see chapter 2.3), because it was not available at the time the studies were made.

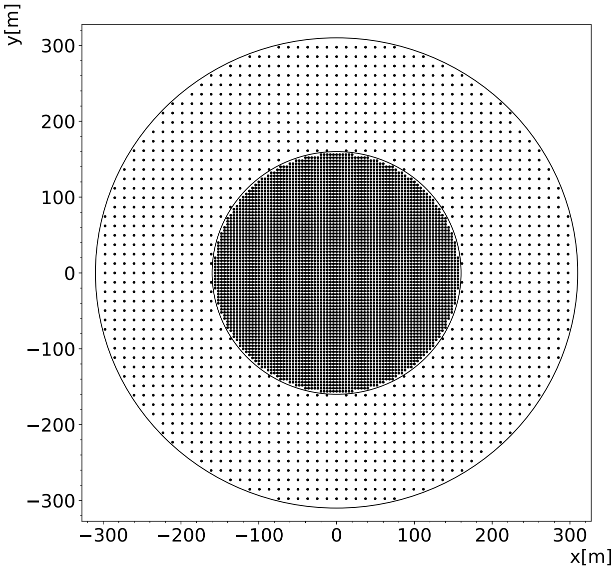

Figure 3.2: Schematic of the realistic layout. The dots represent tanks with a radius of 2 m. There is no difference between the tanks in the outer and the inner array.

3.2 Color Analysis

In this section the influence of the inner wall color on the single tank trigger probability, the number of tanks triggered as well as signal amplitude will be studied. Timing information will not be used in this thesis. However, due to the higher reflectivity of white tanks in comparison to black tanks, the Cherenkov photons can be reflected multiple times on the white walls before arriving at the PMT. So a significant loss in the arrival timing of the first PE is expected, but this study is beyond the scope of this work. Within this chapter tanks with a radius of 2 m and an upper cells height of 3 m are utilized in combination with the two tank color configurations.

3.2.1 Single Tank Trigger Probability

To evaluate the dependency of the trigger effectiveness on the color of the linings, first the single tank trigger probability as a function of the distance from the center of the shower core (impact distance) (r) is used. As all the showers are thrown at the center of the array, here the center of the shower core is the same as the center of the array. The single tank trigger probability is defined as the probability that the tank's PMT at a given distance detects at least one PE. To obtain the probability profile, the column layout, shown in figure 3.1, as well as the simulated air showers, introduced in section 3.1.1 were utilized. In figure 3.3 the profiles for the upper layer of the DLWCDc are shown for the two tank color configurations in different energy bins. In the lower part of the plot the profiles for the relative difference $\frac{P_{\mathrm{White}}-P_{\mathrm{Black}}}{P_{\mathrm{Black}}}$ are shown. As expected the probability is one for distances near to the center of the shower core and decreases with increasing distance. This behavior is stronger for low energies compared to higher ones. It can also be seen from the probability plot, that the white configuration has higher probabilities than the black color configuration at the same distance. The relative difference plot is analyzed for a better understanding of this behavior. Here one can distinguish between distances < 50 m (near to the center of the shower core) and distances > 50 m. At small distances near to the center of the shower core, which is likely the case in the inner array, where the tanks are closely packed, going from black to white for low energies would lead to a gain in the single tank trigger probability up to 50%. There is no significant gain for higher energies.

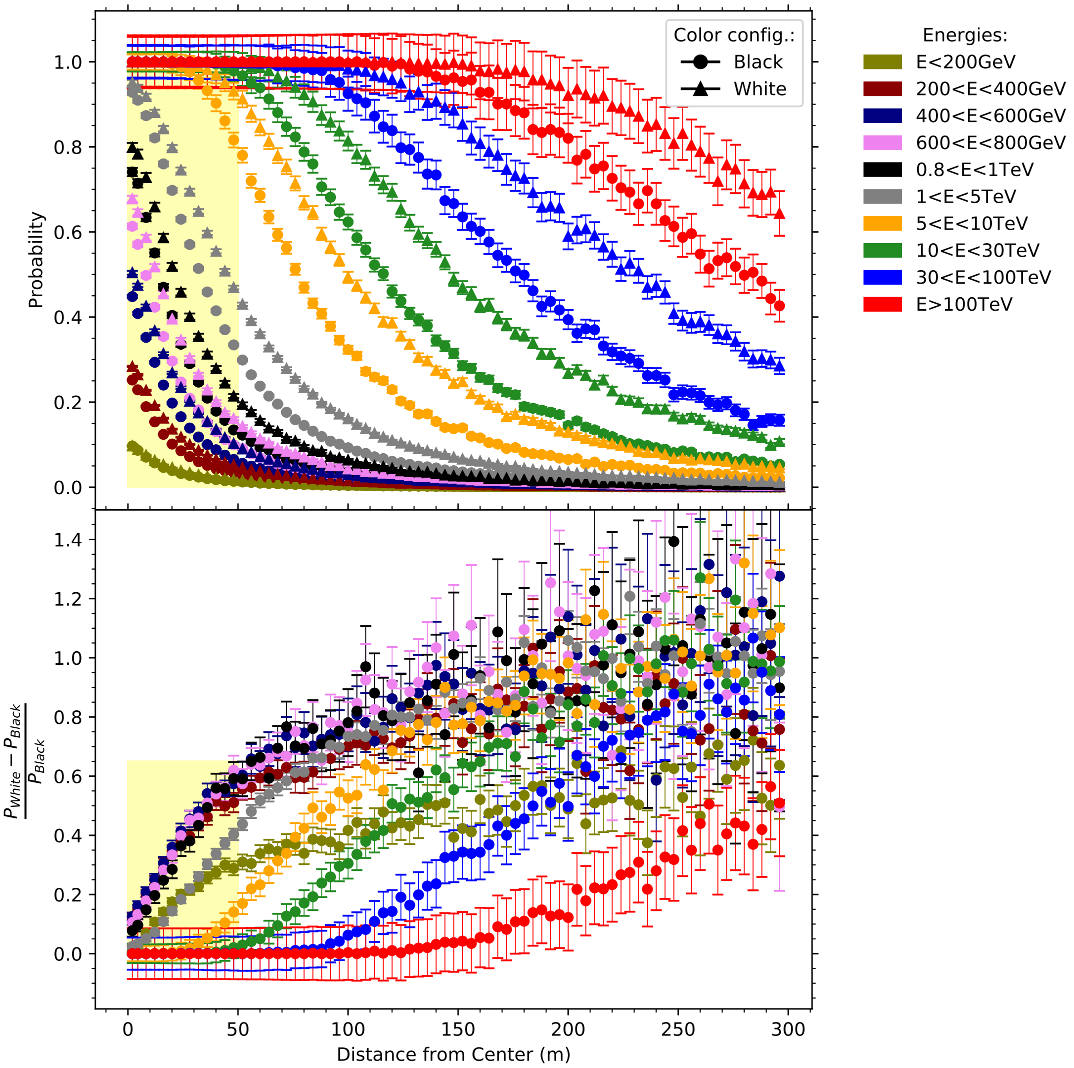

Figure 3.3: Top: at least one PE trigger probability profiles for the upper layer of the DLWCDc. The tank color configurations are black (dot) and white (triangle). The energy is splitted up in 10 bins, which are indicated by different colors. Bottom: the relative difference of the probability (P) for white and black with respect to the probability for black as a function of r. In both cases, the yellow area indicates distances near to the center of the shower core.

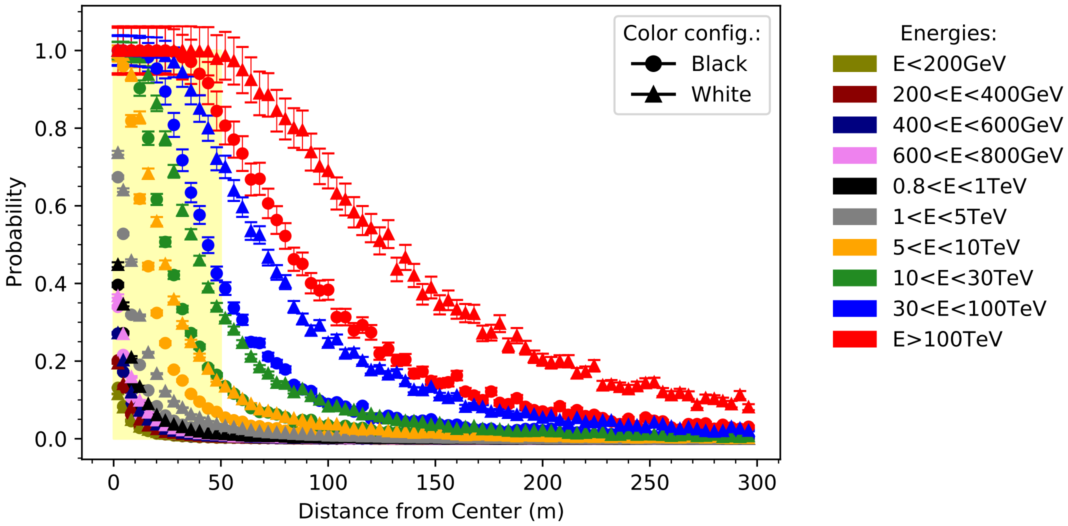

Figure 3.4: At least one PE trigger probability profiles for the lower layer of the DLWCDc. The tank color configurations are black (dot) and white (triangle). The energy is splitted up in 10 bins, which are indicated by different colors. In both cases, the yellow area indicates distances near to the center of the shower core.

Using white instead of black walls at distances more than 50 m would result in a gain of up to 100% for all energies. This would help a lot triggering tanks in the outrigger array. The single tank trigger probability of the lower layer is displayed in figure 3.4. The behavior is the same as already described for the upper layer. The only difference, which is visible it the faster decrease for increasing distance r. Due to the fact that the lower layer of the DLWCDc tank design is only for muon tagging, it is intended to see as much light as possible. Hence white lower layer tank configuration is the appropriate choice.

3.2.2 Number of Tanks Triggered

With the help of the information of the single tank trigger probability one can estimate the number of tanks triggered on the realistic layout. A tank is regarded to be triggered whenever the number of PEs detected with the PMT in the upper layer of the tank is greater than zero. In this section the probability profile for the energy bin $0.6 < E < 0.8$ TeV of the upper layer is used. The profile is convolved with the positions of the tanks of the realistic layout into the information of uniformly distributed simulated shower cores. This method avoids long simulation times.

As shown in figure 3.5 (a), if the shower lands within the array, one will trigger a few hundred tanks in any case even for the low energy bin ($0.6 < E < 0.8$ TeV) and black tank color configuration. Nevertheless a lot more tanks are triggered when using white walls instead of black ones (compare figure 3.5 (a) and (b)), especially at the edge of the array. For higher energies one would trigger even more tanks so that the number a tanks triggered does not seem to be an adequate quantity for the study on the tank design.

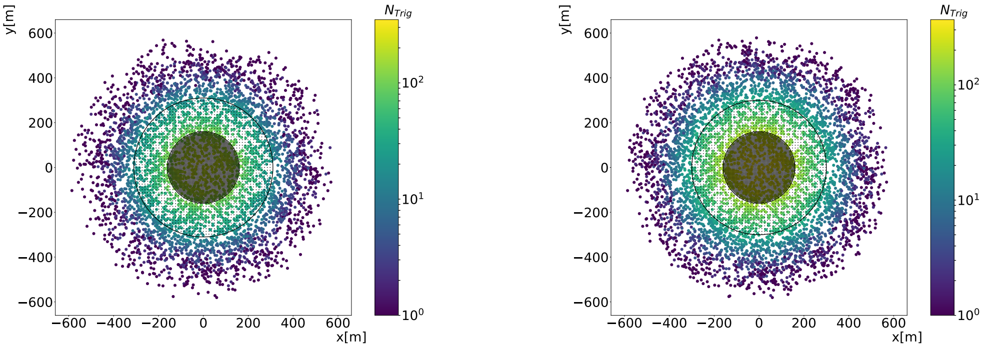

(a) Black tank color configuration

(b) White tank color configuration

Figure 3.5: The number of upper cells got triggered (N_{Trig}) with at least one PE for energy bin $0.6 < E < 0.8$ TeV.

3.2.3 Signal Amplitude Study

Measurements on the signal amplitude at several distances r, allow investigations on the saturation of PMTs. Avoiding saturation is utterly important, because saturation of several PMTs has an adverse effect on the shower reconstruction. Due to saturation, the real signal amplitude information is lost. Therefore, it is of great importance to avoid saturation for a given detector configuration while maximising the signal amplitude to improve the shower reconstruction. The Hamamatsu 8” PMT used within the simulations saturates at about 10,000 PEs. In figures 3.6 and 3.7, this is indicated by a dashed horizontal line. The vertical line in both cases represents a saturation distance, a distance where saturation can be prominent. The saturation distance is in general defined as the minimal distance between two tanks where one is saturated and the other one is not, because of the distance.

In order to get a deeper understanding of saturation, the study of averaged N_{PE} as function of r is performed. Figure 3.6 shows the results of the study for the upper cell, while in figure 3.7 the results for the lower layer are displayed. As can be seen, for the lower layer it can be concluded, that saturation is not a problem, for both the black and the white tank configuration. At low energies there is no saturation at all and at higher energies the saturation distance is less than 8 m. In case of the upper layer saturation becomes an issue. Particularly for the high energies and white configuration, where the saturation distance is 20 m. Changing the color configuration form white to black leads to a decrease in the average N_{PE} at the same distance r. A relative difference plot is shown in figure 3.8, to see the influence of changing the color. Using white tank configuration instead of black would result in a gain of 140% in the average number of PEs for almost all energies for distances > 50 m.

For lower distances the gain is between 70% and 125%. For all studies on the

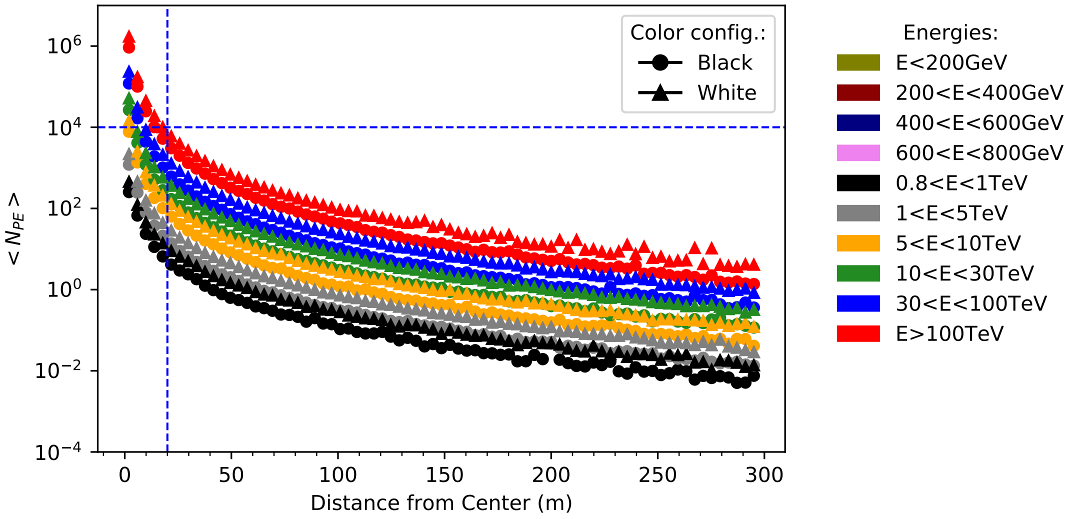

Figure 3.6: The average number of PEs ($\langle N_{\mathrm{PE}} \rangle$) with black and white tank wall color configuration for the upper layer as a function of r for different energies. Saturation of the 8” PMT is indicated by the dashed blue horizontal line. The vertical line represents the saturation distance.

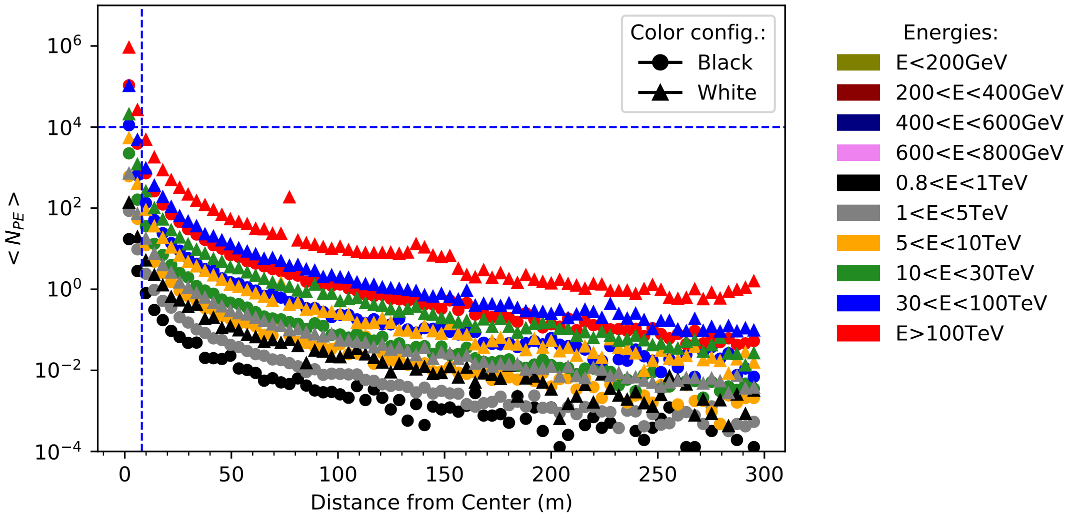

Figure 3.7: The average number of PEs ($\langle N_{\mathrm{PE}} \rangle$) with black and white tank wall color configuration for the lower layer as a function of r for different energies. Saturation of the 8” PMT is indicated by the dashed blue horizontal line. The vertical line represents the saturation distance.

signal amplitude, no error bars are shown because of the large errors. In order to clarify, four histograms (see figure A.1 and A.2), for different distances r and color configurations are shown in the appendix. Within these histograms, the mean ($\langle N_{\mathrm{PE}} \rangle$) and the standard deviation are displayed. The long tail up to high N_{PE}’s, which is responsible for the large errors, appears due to binning in energy. Nevertheless, the $\langle N_{\mathrm{PE}} \rangle$ allows a measure of the overall expected signal amplitude in a certain energy range.

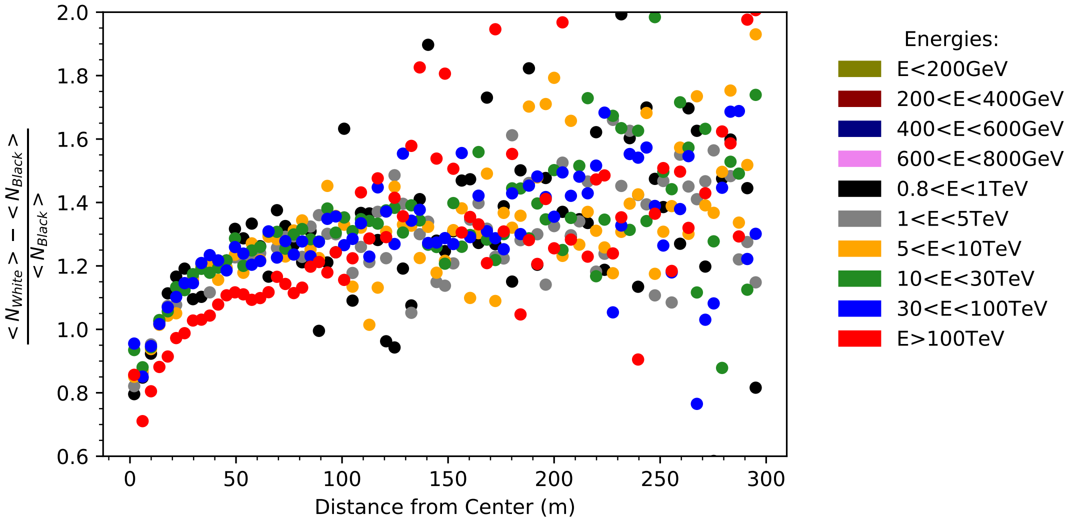

Figure 3.8: Relative difference of the average number of PEs measured with black and white tank color configuration in the upper layer.

3.3 Height Analysis

Avoiding saturation is not only possible by changing the color of the tanks walls, but also by increasing the height. For this reason, three different upper cells heights in combination with a tank radius of 2 m and the black tank configuration are used, in this section, in order to examine the saturation and thus the average number of PEs more in detail. After this, the single tank trigger probability is observed to check whether the triggering capability of the tanks is influenced negatively or positively.

3.3.1 Signal Amplitude Study

To see an influence of the upper layers height on the average number of PEs two energy ranges from 1 TeV to 5 TeV and from 30 TeV to 100 TeV were chosen. The range $1 < E < 5$ TeV thereby represents lower energies and the energy range $30 < E < 100$ TeV is chosen for studies on higher energies. The results are shown in figure 3.9 and 3.10. From the upper part of these plots, it can be seen, that changing the height of the upper layer, not only effects the signal in the upper cell, but also has an influence on the measured signal in the lower layer. The lower part of the plots shows the relative difference $\frac{N_{down}-N_{up}}{N_{up}}$ for the different heights. For both analyzed energy ranges, the same behavior is observed. Comparing the average number of PEs detected in the upper layer to one in the lower layer, a loss of 96% in the lower layer with respect to the upper layer for a upper cells' height of 2 m is observed, respectively 98% for a height of 3 or 4 m. This represents the expected behavior, that with increasing upper layers height less particles reach the lower layer and so less secondary particles are produced and the PMTs therefore detect lesser PEs. The second information, which comes up by looking at the upper part of the plots is, that the average number of PEs is decreasing in the upper as well as the lower layer with increasing height. In figure 3.11 and 3.12

the relative differences $\frac{N_{3m}-N_{2m}}{N_{2m}}$ and $\frac{N_{4m}-N_{3m}}{N_{3m}}$ are plotted as a function of r for the upper layer. Both relative difference curves, for the two analyzed energy ranges, follow the same behavior. Going from 2 m to 3 m or from 3 m to 4 m gives a loss in the average number of PEs of up to 40% and 55% at least near to the shower core. At larger distances from the shower core, even though statistical fluctuations starts to dominate, nevertheless a loss in observed signal is visible, especially for the relative difference (3 m → 4 m).

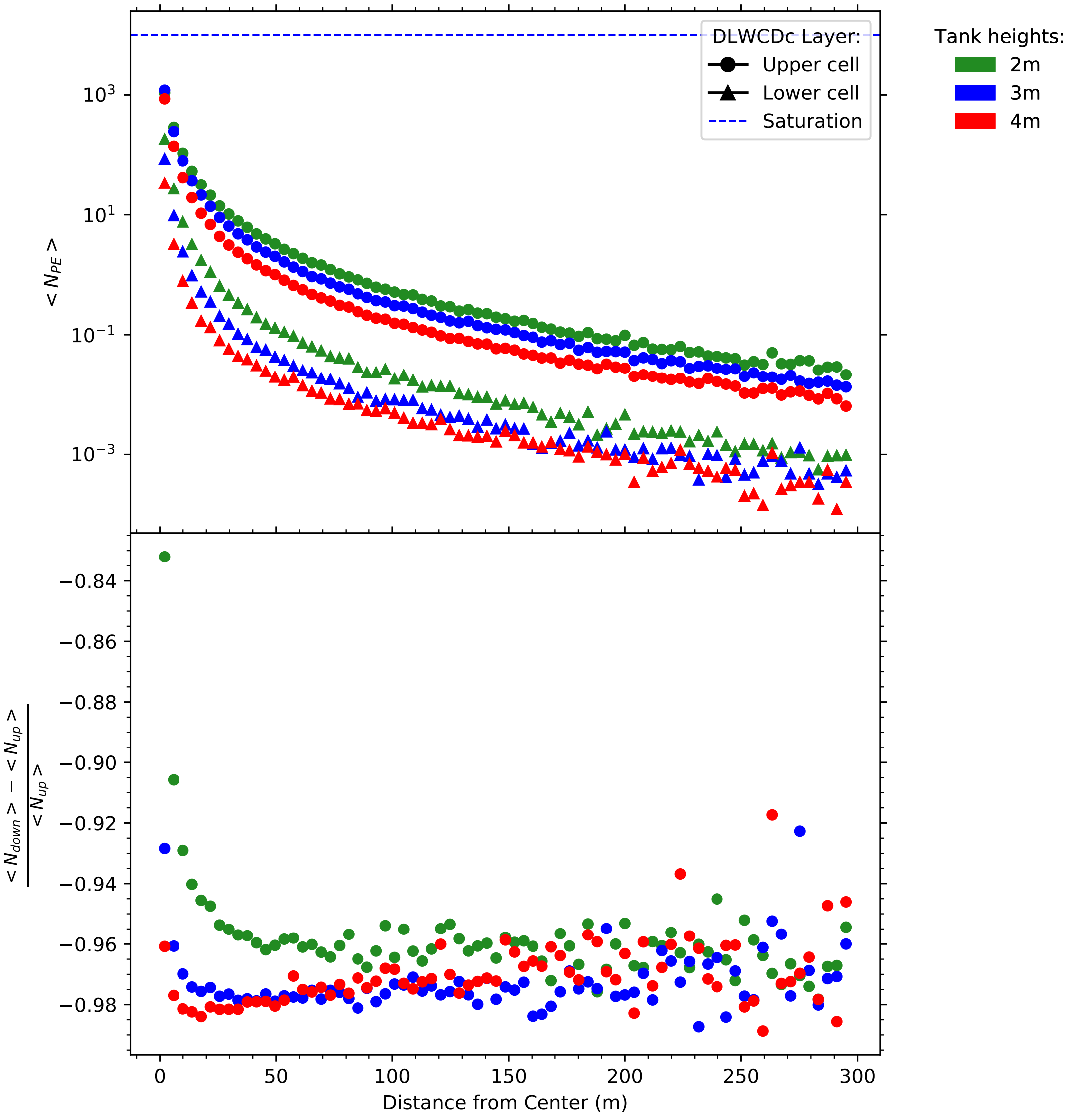

Figure 3.9: Top: The average number of PEs ($\langle N_{\mathrm{PE}} \rangle$) for $1 < E < 5$ TeV with black tank wall color configuration for the upper and the lower layer as a function of r for different upper cells heights. Bottom: Relative difference of the average number of PEs measured within the upper and the lower layer.

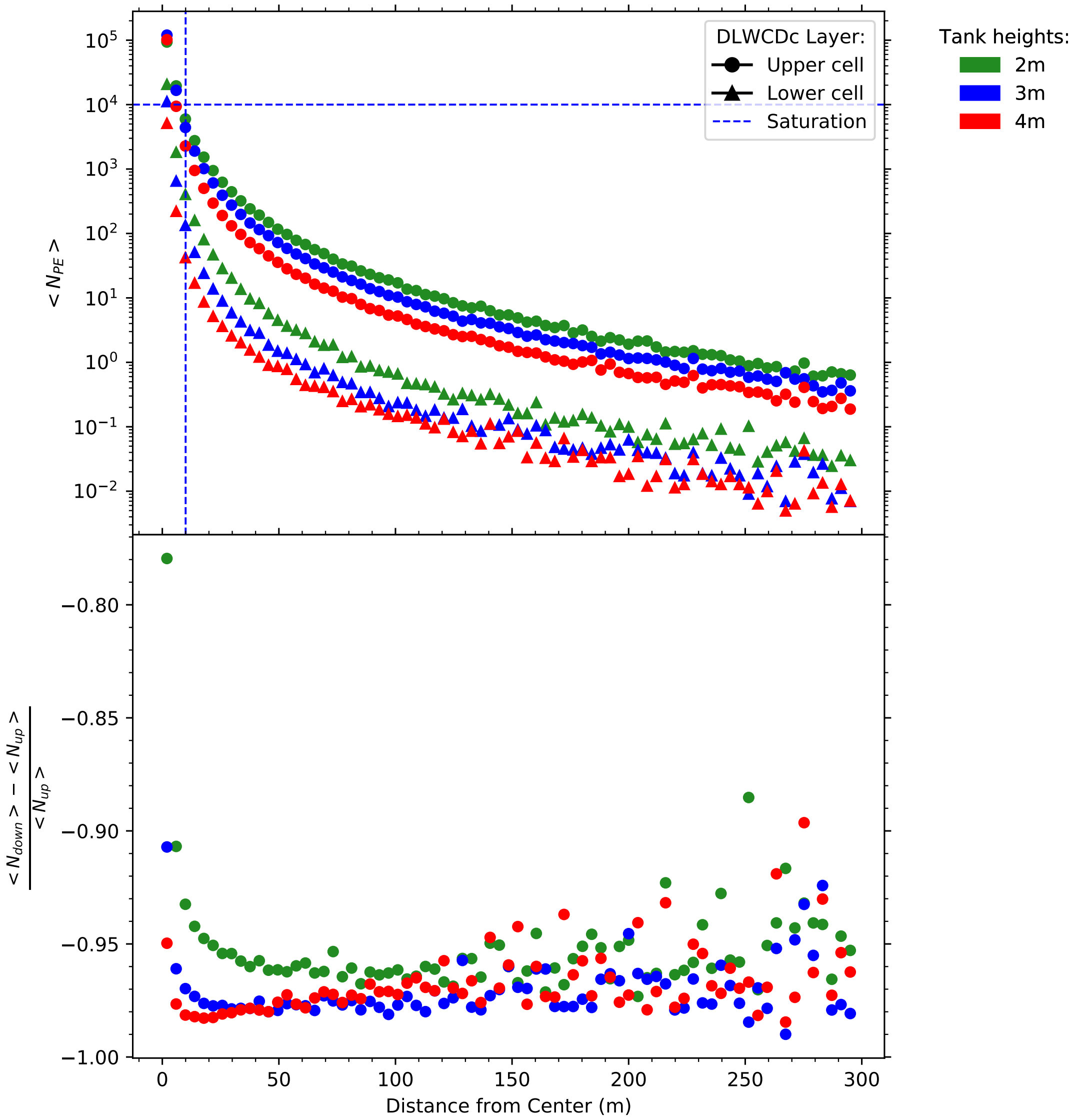

Figure 3.10: Top: The average number of PEs ($\langle N_{\mathrm{PE}} \rangle$) for $30 < E < 100$ TeV with black tank wall color configuration for the upper and the lower layer as a function of r for different upper cells heights. Bottom: Relative difference of the average number of PEs measured within the upper and the lower layer.

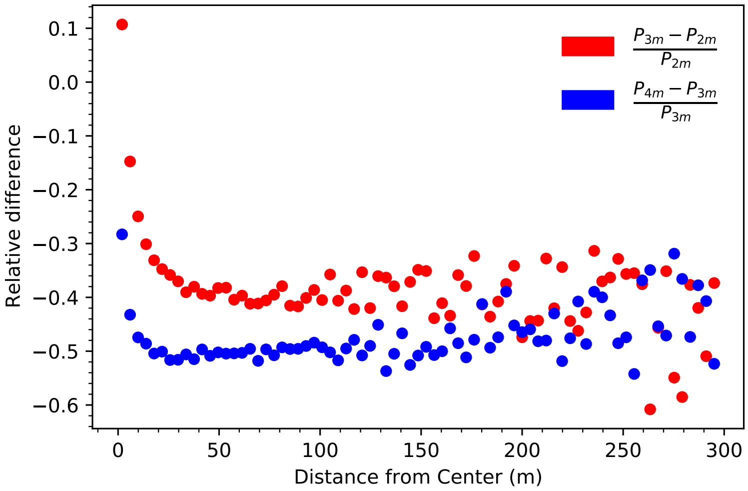

Figure 3.11: Relative difference of the average number of PEs measured for 2, 3 and 4 m upper cells heights. The results are for the upper layer and an energy range of $1 < E < 5$ TeV.

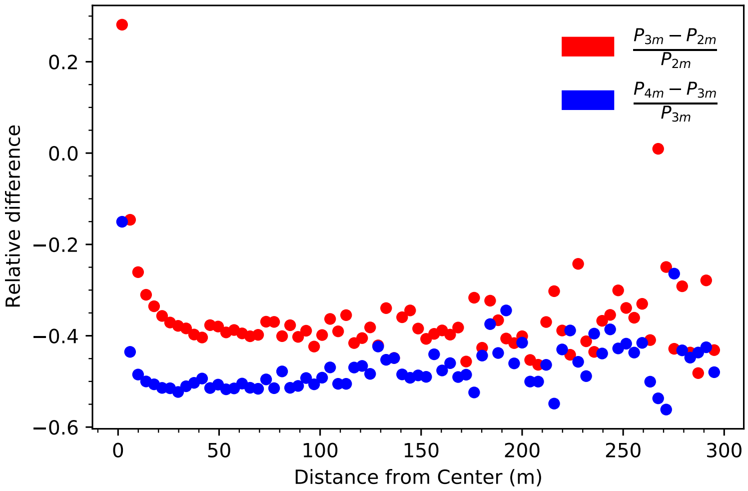

Figure 3.12: Relative difference of the average number of PEs measured for 2, 3 and 4 m upper cells heights. The results are for the upper layer and an energy range of $30 < E < 100$ TeV.

3.3.2 Single Tank Trigger Probability

The signal amplitude study for different heights showed that saturation can be reduced by increasing the upper cell height. But it is also important evaluate the influence on the single tank trigger probability. As discussed in chapter 2.1 the geometry of the tank plays an important role in the detection of Cherenkov light. Particularly for lower energies and high tank heights, the probability to trigger tanks has to be observed, to ensure that enough tanks are triggered. In the upper part of figure 3.13 the single tank trigger probability of the upper layer for an energy range form 1 to 5 TeV is analyzed.

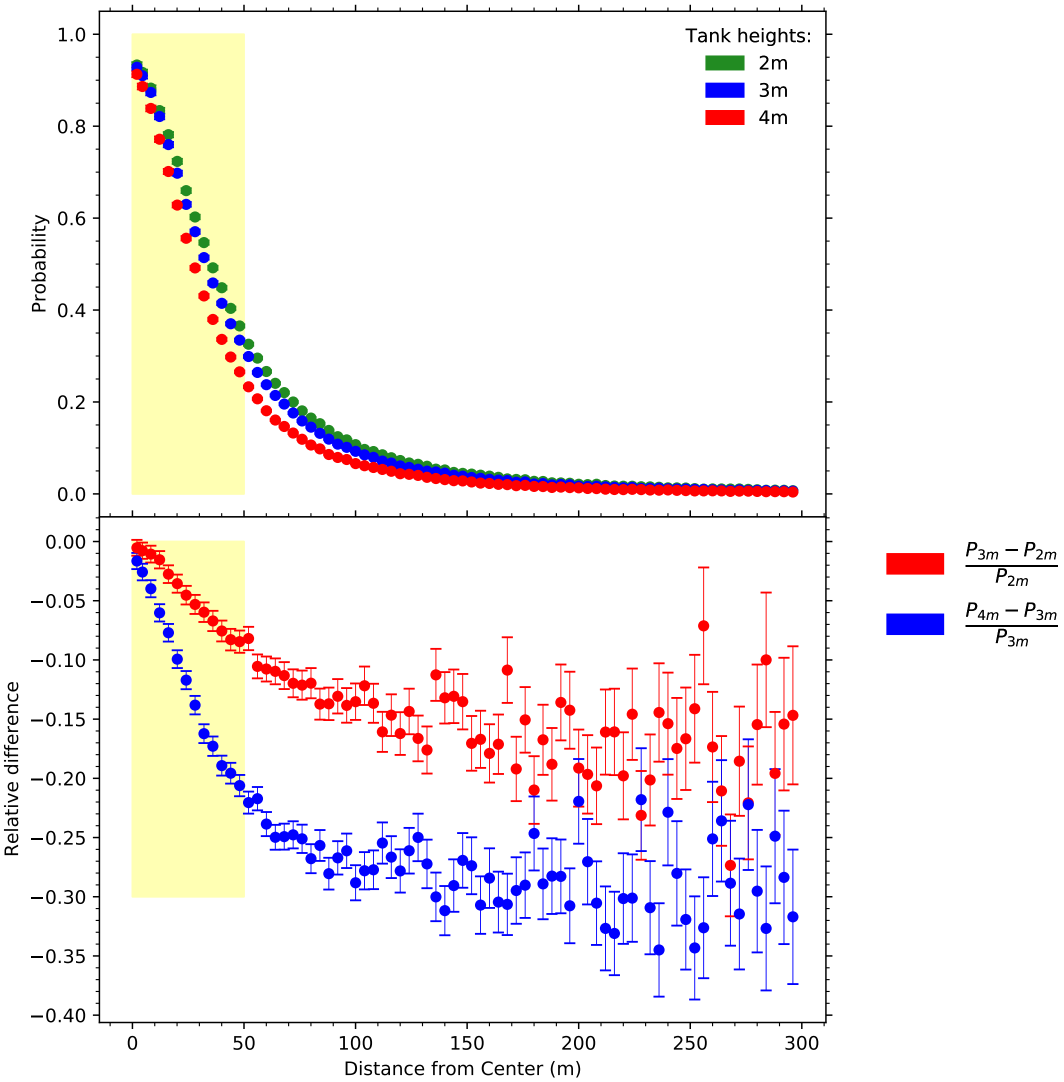

Figure 3.13: Top: at least one PE trigger probability profiles for the upper layer of the DLWCDc. The compared tank heights are 2, 3 and 4 m. The energy range is $1 < E < 5$ TeV. Bottom: the relative difference of the probability (P) for increasing tank height as a function of r. In both cases, the yellow area indicates distances near to the center of the shower core.

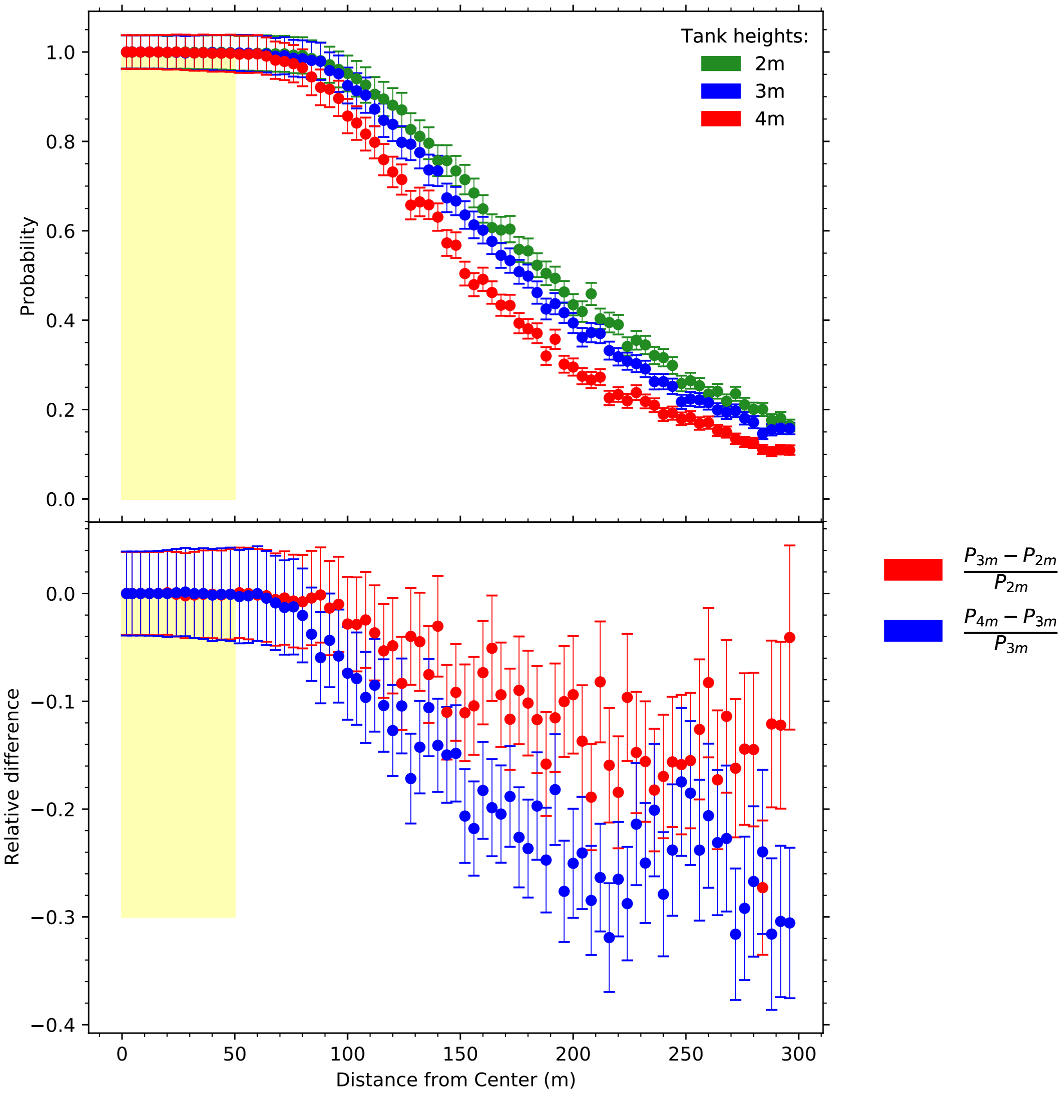

Figure 3.14: Top: at least one PE trigger probability profiles for the upper layer of the DLWCDc. The compared tank heights are 2, 3 and 4 m. The energy range is $30 < E < 100$ TeV. Bottom: the relative difference of the probability (P) for increasing tank height as a function of r. In both cases, the yellow area indicates distances near to the center of the shower core.

Compared to the single tank trigger probability for $30 < E < 100$ TeV, which is shown in the upper half of figure 3.14, the probability decreases much faster with increasing r. This was already discussed in section 3.2. Furthermore it can be seen, that the single tank trigger probability is decreasing with increasing tank height. This expected behavior is analyzed more closly in the lower parts of figure 3.13 and 3.14. In both cases the relative difference $\frac{P_{3m}-P_{2m}}{P_{2m}}$ and $\frac{P_{4m}-P_{3m}}{P_{3m}}$ is plotted as a function of r for the upper layer. For distances < 50 m (displayed through the yellow box) and high energies ($30 < E < 100$ TeV), there is no significant loss, when increasing the tank height. For the energy range $1 < E < 5$ TeV, which represents a lower energy range, there is a loss up to 8% for the relative difference

(2 m → 3 m). When going from 3 to 4 m a loss of 23% can be determined. For distances higher than 50 m there is nearly the same behavior for all energies. A loss of approximately 20% is observed when going from 2 m to 3 m in height. A further loss of 30% is observed in the single tank trigger probability, while increasing the tank height from 3 m to 4 m.

3.4 Radius Analysis

The third tank parameter, which is under investigation in this thesis is the tank radius. For this study again the column layout is used in combination with the black tank color configuration and an upper cell height of 3m. On the one hand, with increasing radius it is expected to be able to increase the single tank trigger probability due to a larger volume. On the other hand the average number of PEs is also expected to increase. In the following execution both, the single tank trigger probability and the average number of PEs are under investigation for a better understanding. Again two energy ranges from 1 TeV to 5 TeV and from 30 TeV to 100 TeV were used for the study. The range $1 < E < 5$ TeV thereby represents lower energies and the energy range $30 < E < 100$ TeV is chosen for studies on higher energies.

3.4.1 Single Tank Trigger Probability

To see the dependency of the trigger effectiveness on the tank radius the single tank trigger probability as a function of distance from the shower core is used. For more information on the definition of the single tank trigger probability see section 3.2.1. The column layout, shown in figure 3.1, as well as the simulated air showers, introduced in section 3 were utilized to obtain the probability profile. Figure 3.15 and 3.16 show the profiles for the upper layer of the DLWCDc for the tank radii 1, 2 and 3 m. The profiles for the relative difference of the probability $\frac{P_{3m}-P_{2m}}{P_{2m}}$ and $\frac{P_{2m}-P_{1m}}{P_{1m}}$ are shown in the lower part of the plot. By looking at one radius only, i.e. 2 m the behavior of the profile is the same as in figure 3.3. The probability is one for distances near to the center of the shower core and decreases with increasing distance. This behavior is stronger for low energies compared to the higher ones.

The new information from the probability profiles is the confirmation of the expectations. The probability increases with increasing tank radius at the same distance r. Looking at the plots in the lower part of figure 3.15 and 3.16 it can be seen that the relative difference is positive, which is equivalent to improvement of trigger capability. For small distances < 50 m near the shower core, which is most likely the case in the inner array, where the tanks are closely packed, going from 1 m to 2 m for low energies ($1 < E < 5$ TeV) would lead to a gain up to 20%. This effect is even higher, $\sim 55\%$, when increasing the tank height from 2 m to 3 m. For distances > 50 m the gain approaches up to 70% for both, going from 1 m to 2 m and from 2 m to 3 m. Compared to this, the behavior is different for higher energies ($30 < E < 100$ TeV) especially near to the center of the shower core. In the region < 50 m no significant gain is visible for both cases (1 m → 2 m) and (2 m → 3 m). The relative difference increases up to a value of 0.5 to 0.6 at distances higher than 200 m. In other words, increasing the tank radius by 1 m, from 1 m to 2 m, or from 2 m to 3 m, would result in an increase of between 50% and 60% in the trigger probability for a single tank at distances greater than 200 m.

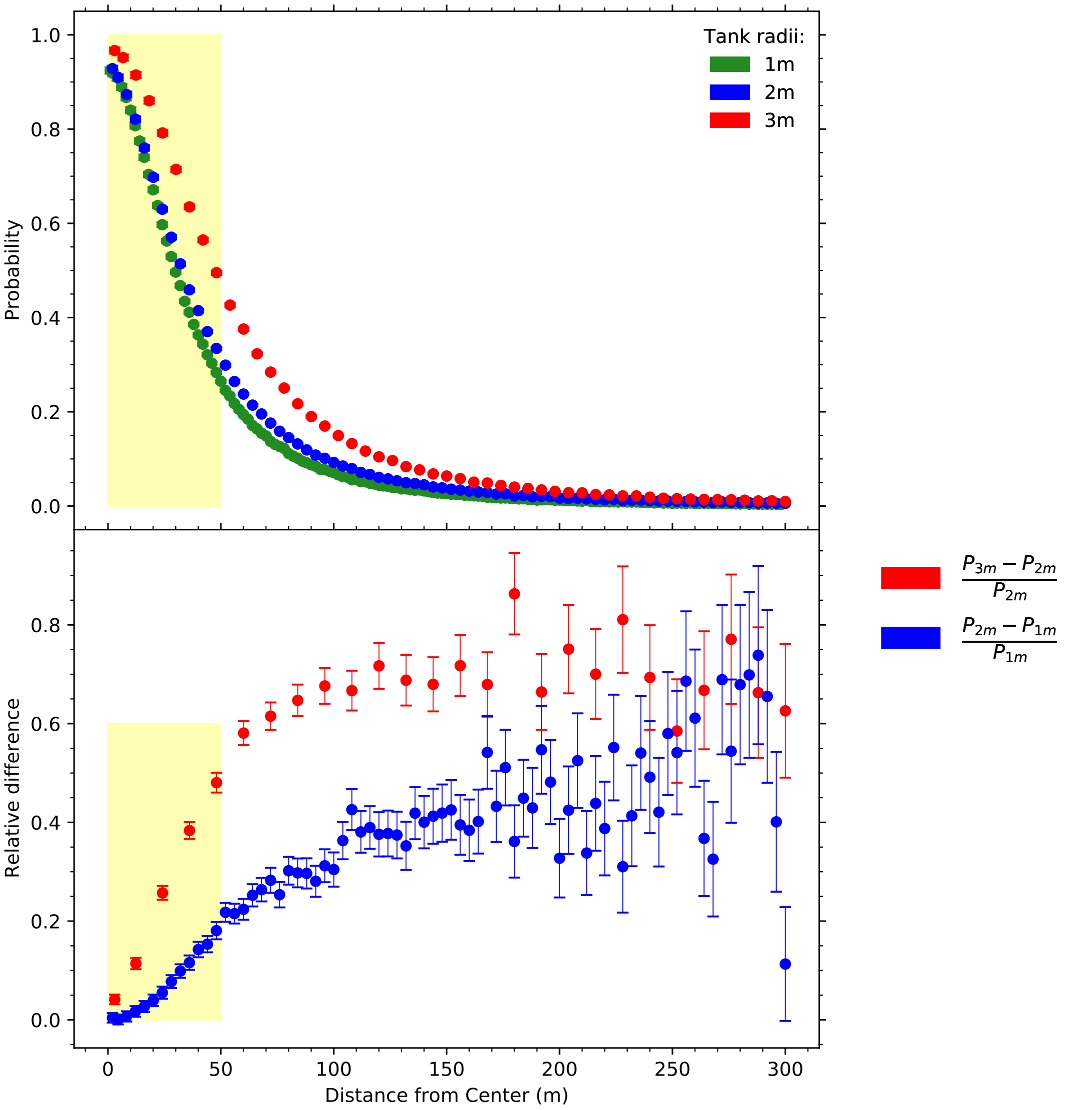

Figure 3.15: Top: at least one PE trigger probability profiles for the upper layer of the DLWCDc. The compared tank radii are 1, 2 and 3 m. The energy range is $1 < E < 5$ TeV. Bottom: the relative difference of the probability (P) for increasing tank radius as a function of r. In both cases, the yellow area indicates distances near to the center of the shower core.

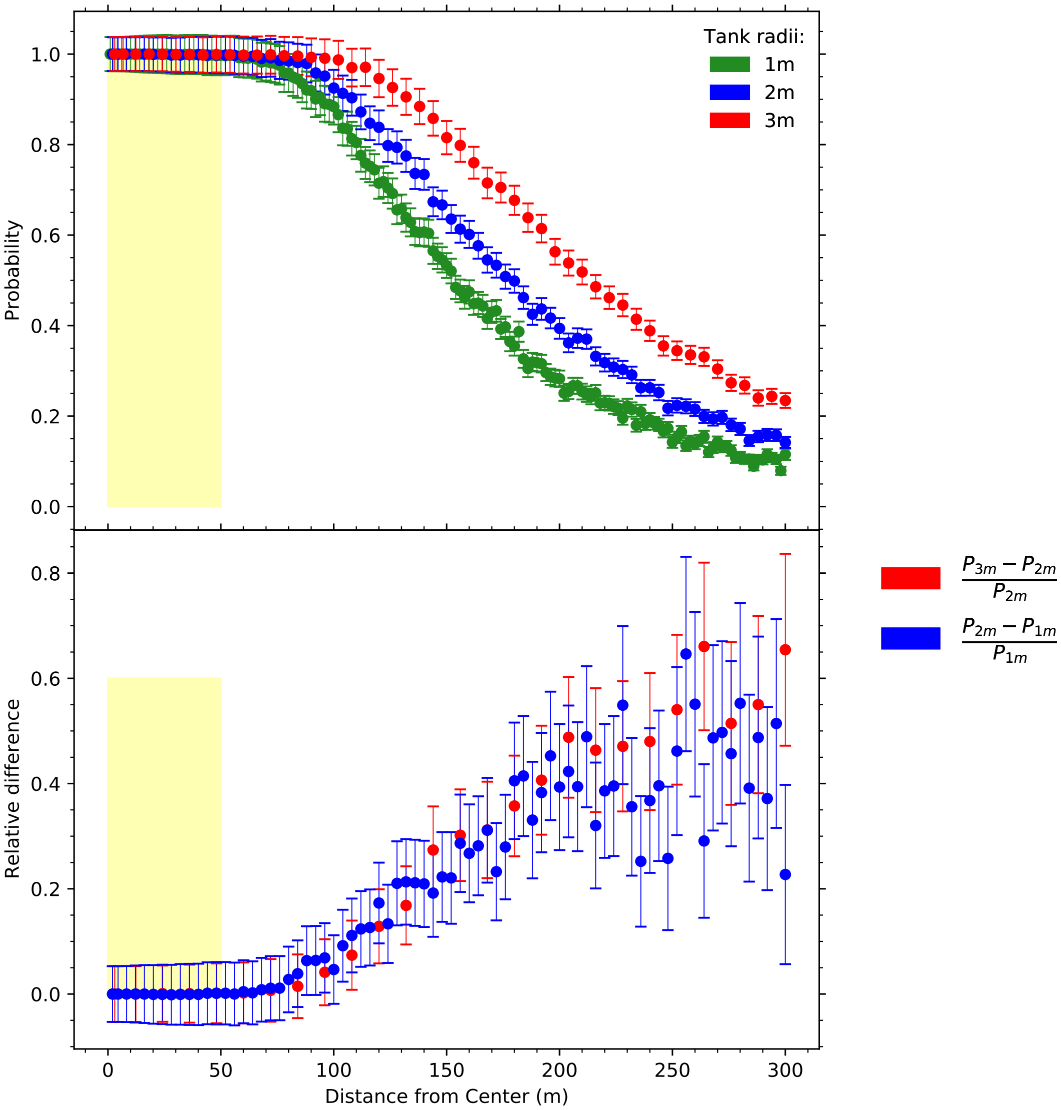

Figure 3.16: Top: at least one PE trigger probability profiles for the upper layer of the DLWCDc. The compared tank radii are 1, 2 and 3 m. The energy range is $30 < E < 100$ TeV. Bottom: the relative difference of the probability (P) for increasing tank radius as a function of r. In both cases, the yellow area indicates distances near to the center of the shower core.

3.4.2 Signal Amplitude Study

As already described in chapter 3.2.3 the measurements on the signal amplitude at several distances from the shower axis r, allow investigations on the saturation of PMTs. Avoiding saturation for a given detector configuration while maximizing the signal amplitude is of great significance to improve the shower reconstruction. Therefore simulations with three different tank radii (1 m, 2 m and 3 m) were made in order to look at the average number of PEs. The results can be seen in figure 3.17 and 3.18. From the upper part of these plots, it becomes clear that changing the radius, not only effects the signal in the upper cell, but also has

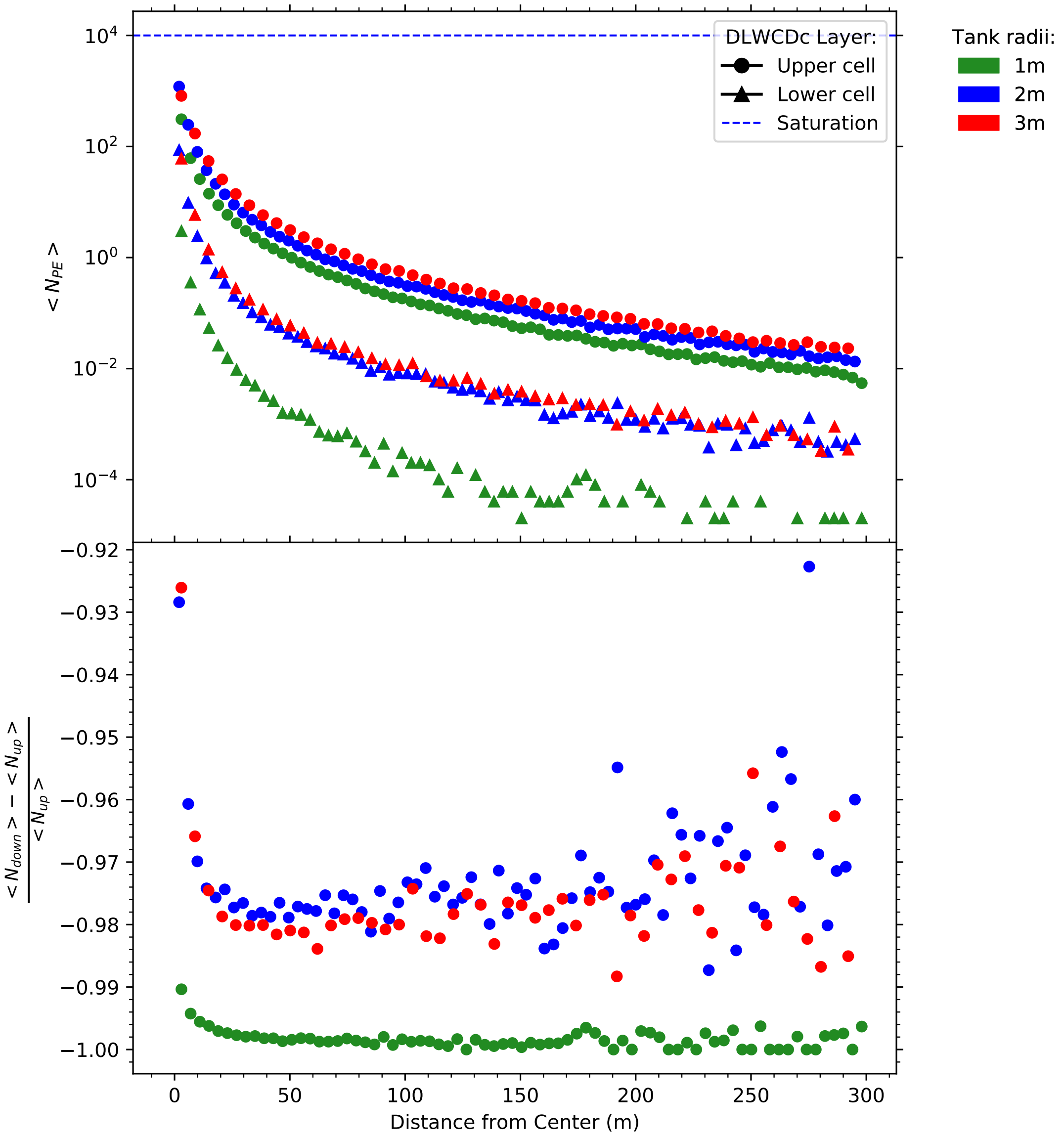

Figure 3.17: Top: The average number of PEs ($\langle N_{\mathrm{PE}} \rangle$) for $1 < E < 5$ TeV with black tank wall color configuration for the upper and the lower layer as a function of r for different tank radii. Bottom: Relative difference between the average number of PEs measured within the upper and the lower layer.

an influence on the measured signal in the lower layer. By having a look at the lower part of the plot, this becomes more obvious. Here the relative difference $\frac{N_{\text{down}}-N_{\text{up}}}{N_{\text{up}}}$ is shown for the different radii. The same behavior is discovered for both analyzed energy ranges. For a radius of 1 m there is a loss of about 100%, when comparing the average number of PEs in the lower with respect of the the upper layer. For a radii 2 m and 3 m the relative difference is not that high. Here is a loss of 98% visible. Further it can be seen that the average number of PEs decreases with decreasing tank radius, in both layers separately.

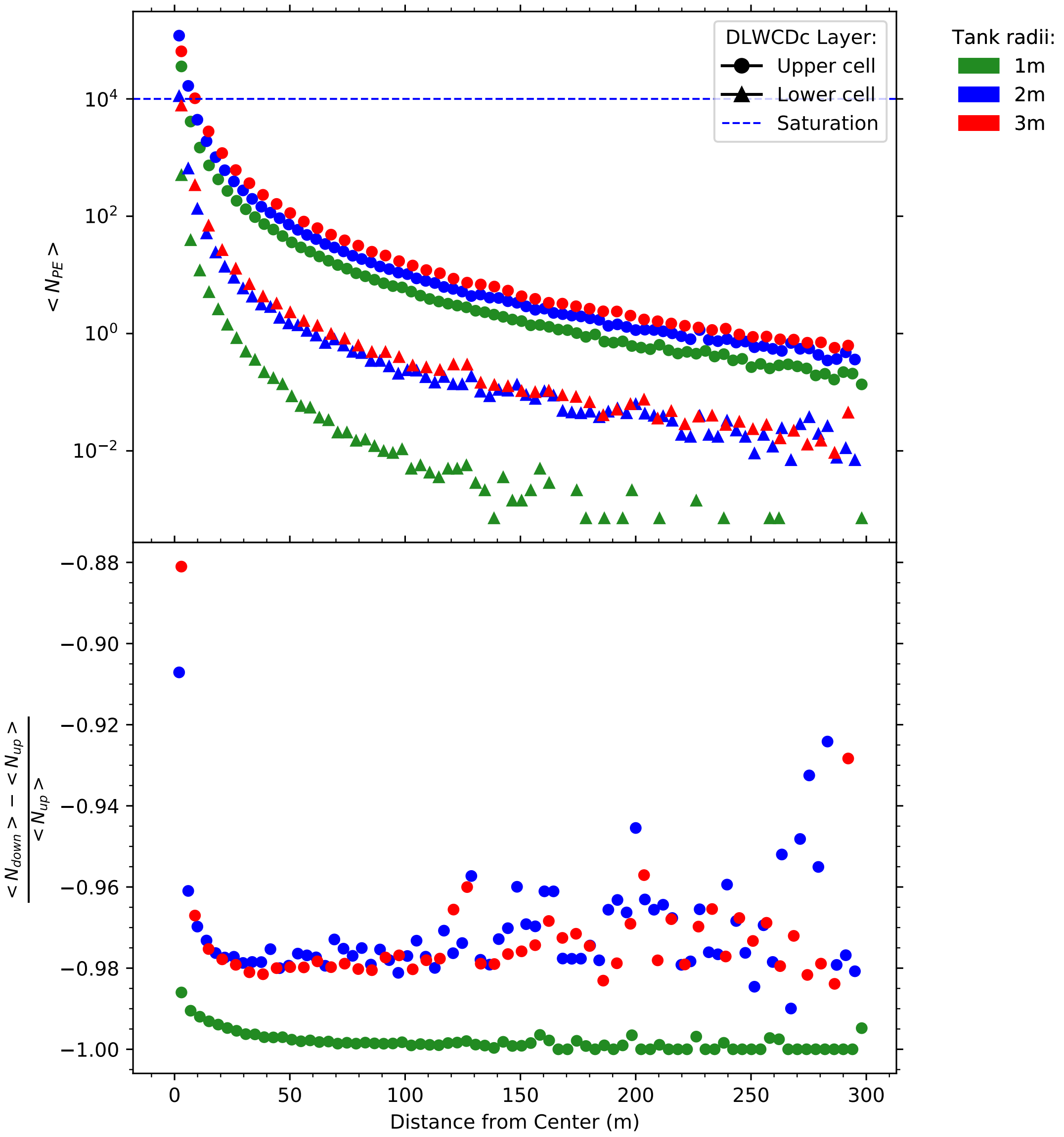

Figure 3.18: Top: The average number of PEs ($\langle N_{\text{PE}}\rangle$) for $30 < E < 100$ TeV with black tank wall color configuration for the upper and the lower layer as a function of r for different tank radii. Bottom: Relative difference between the average number of PEs measured within the upper and the lower layer.

In figure 3.19 and 3.20 the relative differences $\frac{N_{3m}-N_{2m}}{N_{2m}}$ and $\frac{N_{2m}-N_{1m}}{N_{1m}}$ for the upper layer are plotted for the two given energy ranges. From these plots it can be concluded that the relative difference is energy independent. In both shown energy ranges there is a gain of at least 100% in the average number of PEs for tanks with a radius of 2 m with respect to tanks with a radius of 1 m. The gain in case of increasing the tank radius from 2 m to 3 m, is above 50%.

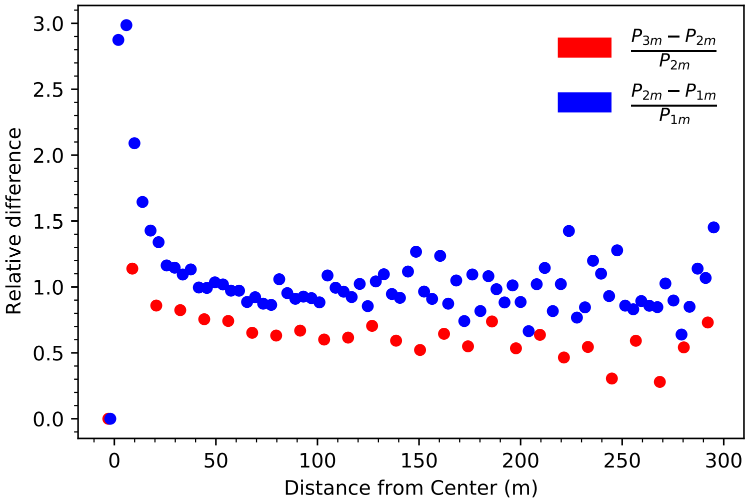

Figure 3.19: Relative difference between the average number of PEs measured for 1, 2 and 3m tank radii. The results are for the upper layer and an energy range of $1 < E < 5TeV$.

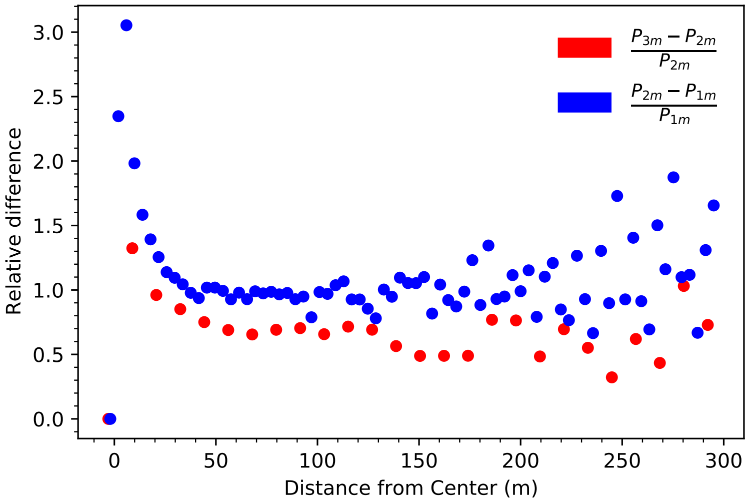

Figure 3.20: Relative difference between the average number of PEs measured for 1, 2 and 3 m tank radii. The results are for the upper layer and an energy range of $30 < E < 100$ TeV.

3.5 Conclusion

Different tank designs of the DLWCDc were introduced and analyzed in this chapter. Tanks with two inner wall color configuration, as well as three tank radii and three different upper cell heights were simulated to decide on a suitable tank configuration. Results shown in sections 3.2, 3.3 and 3.4, suggest the following:
Increasing the tank height to at least 3 m or 4 m, for low energies, lead to a loss in trigger probability. This could be compensated by using a larger radius, e.g 2 m or 3 m. Additionally, this also could be done using white color configuration for the upper cell. At low energies, saturation is not a problem. For this reason, one do not need to decide the configuration upon the average number of PEs. For high energies the single tank trigger probability is not a problem, which means one will trigger enough tanks for shower reconstruction regardless of the tank dimensions and the color configuration. On the one hand, using black tank color configuration and high heights would help to avoid saturation near to the shower core. On the other hand, going from black to white will help in receiving more signal at larger distances from the core.
For the lower cells, white walls would lead to a significant increase in trigger probability and signal amplitude. Due to the fact that the lower cell will be most likely used for muon tagging, it is advantageous to use white walls, to be able to supply the lower cells PMT with as much light as possible.
The decision on the tank dimensions strongly depends on the costs. In general, higher and larger tanks will lead to rising costs. An other issue, which has to be taken into account is transportation. If the tanks are built at the location of SWGO, there will be no problem. But if the tanks are built somewhere else, the size, especially the radius, is limited by the mode of transport. Based upon this, the choice of the tank dimensions will lead to small tank designs, which show the best results. Hence, the recommendation for the inner array tank layout would be tanks with a radius of 2 m and a height of 4 m to avoid saturation at the closely packed inner array. The upper cell should be built with black color configuration, while the lower cell as discussed above, should have a white inner wall lining. For the outer array due to cost reduction the height could be reduced. Here the tanks are sparsely packed so that saturation does not play that important role. More crucial here is the trigger probability, which could be increased by using white walls for the upper cell.

4 γ-Hadron Separation

Hadronic cosmic rays are the most common particles producing air showers which will be detectable by SWGO and therefore represent major background for high-energy γ-ray observation. Hence an effective γ-hadron separation strategy is required. As already discussed in chapter 1.3.3, air showers produced by high-energy CRs and γ-rays differ a lot in their secondary particles and their compactness. Summed up on the one hand γ-ray showers are pure electromagnetic showers with very scarce muons or pions. On the other hand hadronic cosmic rays produce hadronic showers which include a lot of pions, muons and other hadronic secondaries. In the past EAS particle detector arrays were built, utilizing WCDs with one layer. One example for such an array is HAWC, which became fully operational in the year 2015. In HAWC two parameters were defined, called Compactness and Parameter for Identifying Nuclear Cosmic-rays (PINC), using the lateral distributions of the shower. There is nothing against using these two parameters for SWGO as well. These separation methods can be combined even more with new ones, which will come up with new tank designs. One of these tank designs is the DLWCDc, which is introduced in chapter 2.1. The double layer design provides a new separation power, which will be introduced in the following. Subsequently the γ-hadron separator will be optimized.

4.1 Introduction to γ-Hadron Separation using Double Layer Tanks

The typical muon energy in air showers is on the order of a few GeV (Abreu et al. 2019). At these energies muons supposed to travel straight through both top and bottom chambers, depositing a significant amount of Cherenkov light in both. High-energy gamma rays and electrons will cascade in the top chamber and only a small fraction (if any) of this cascade can make it to the bottom chamber. The two behaviors are displayed in figure 4.1.

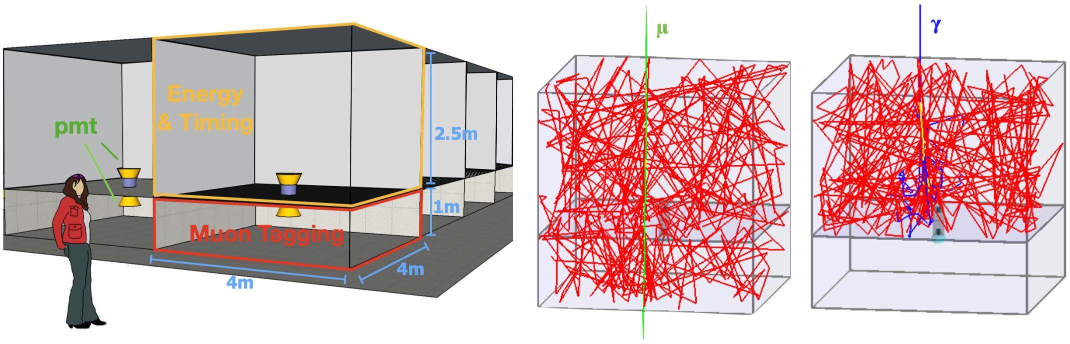

Figure 4.1: Illustration of detection unit design. Right: Muon and gamma-ray passing through a detection unit. Red lines indicate a fraction of the Cherenkov photon tracks, while the green, blue and yellow lines respectively indicate the tracks of muons, gamma rays and electrons. (Image from Abreu et al. 2019)

4.1.1 Motivation for a γ-Hadron Separator using Double Layer Tanks

The relative difference between the detected light in the top and bottom chamber can be used for the identification of muons and therefore γ-hadron separation. Based on the studies made in chapter 3, first a look into the average number of PEs was taken. 500,000 proton and gamma induced CORSIKA showers were used for this to simulate the response of 302 DLWCDcs arranged in the previously introduced column layout. For this first analysis all showers were exactly thrown at the center of the column array. The applied DLWCDcs design can be found in table 4.1.

	Upper layer	Lower layer
Wall lining	Polypropylene	Tyvek
Cover lining	Polypropylene	Tyvek
Bottom lining	Polypropylene	Tyvek
Height [m]	3.0	0.75
Radius [m]	2.0	2.0
PMT sizes	8”	8”

Table 4.1: Tank configuration of the DLWCDc used for γ-hadron separation in combination with the column layout.

In the upper part of figure 4.2 the average number of PEs as a function of distance from the center of the shower core is shown for different particles, energies as well as for the upper and the lower layer. As can be seen the difference between the upper and the lower layer depends a lot on the particle and the observed energy range. Particularly when looking at one energy range e.g. $30 < E < 100$ TeV, it is visible that the gap between the measured $\langle N_{\mathrm{PE}} \rangle$ in the upper and the lower layer for gamma showers (displayed in gray) is much broader compared to proton induced showers (displayed in orange). In order to look into the difference more in detail a plot with the relative difference $\frac{N_{\mathrm{up}}-N_{\mathrm{down}}}{N_{\mathrm{down}}}$ is made. This plot is displayed in the lower part of figure 4.2. Surprisingly, the relative difference for the three representative energy ranges is nearly the same for one primary particle. For γ-rays the value for the relative difference is between 4 and 6 near to the center of the shower core. For more distant tanks (>100 m) the relative difference decreases below 4 and spreads more and more. Proton induced shower result in a relative difference below 2 for all distances and energies.

These results allow to draw some conclusions. First, gamma and hadron induced EASs can be distinguished, using the the relative difference $\frac{N_{\mathrm{up}}-N_{\mathrm{down}}}{N_{\mathrm{down}}}$. Secondly, a distance dependent γ-hadron separator could help to improve the separation effectiveness. Third, it could be concluded that there is no need of an energy dependency of the relative difference threshold, what will turn out to be wrong and will be shown later in this chapter. For a better understanding and to check these proposals the next chapter deals with the relative difference and a distance dependency.

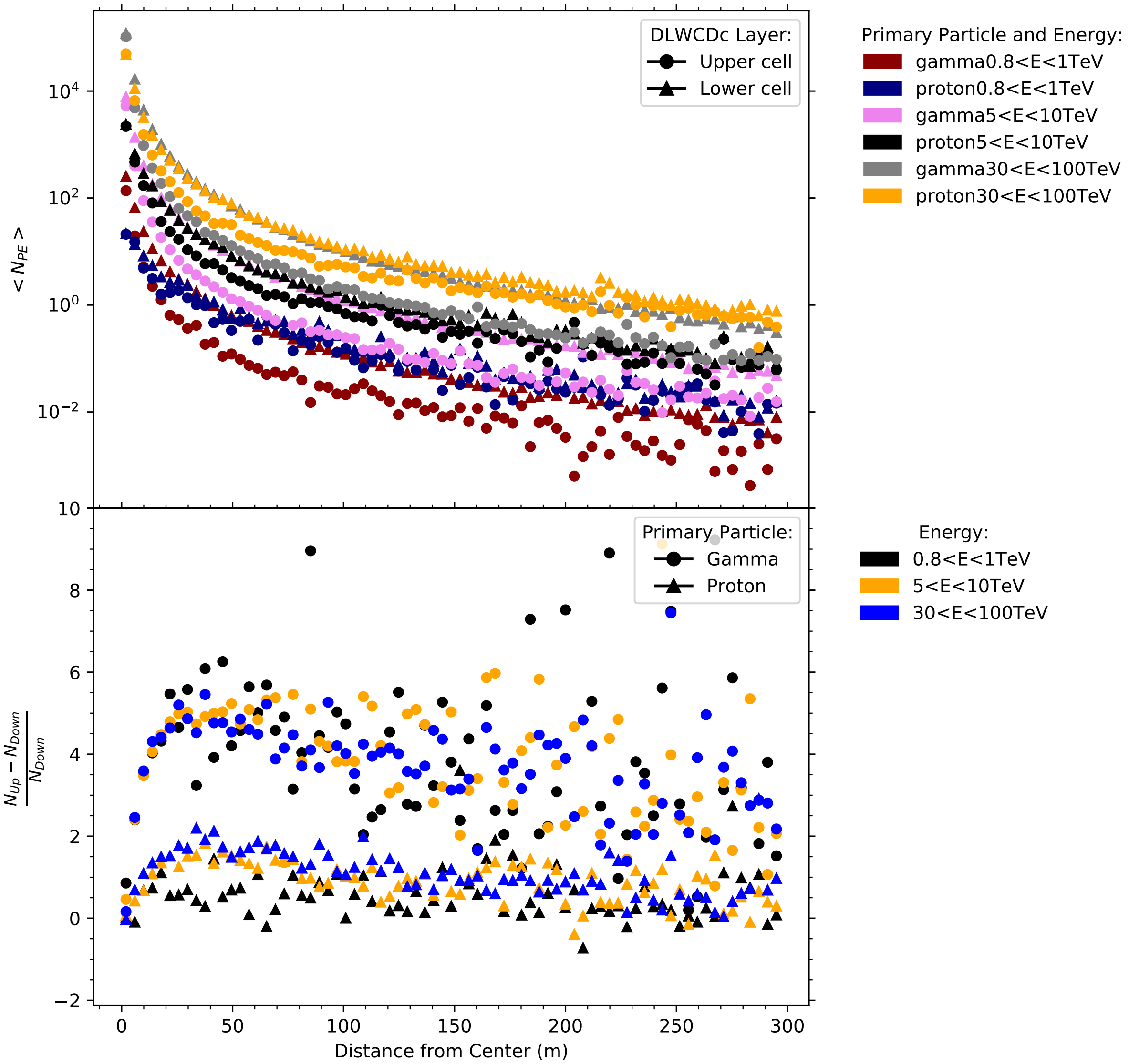

Figure 4.2: Top: The average number of PEs ($\langle N_{\mathrm{PE}} \rangle$) for three representative energy ranges for gamma and hadron induced EASs as well as for the upper and the lower layer as a function of r. Bottom: The relative difference $\frac{N_{\mathrm{up}}-N_{\mathrm{down}}}{N_{\mathrm{down}}}$ between the average number of PEs measured within the upper and the lower layer for different particles and energy ranges.

4.1.2 Distance Dependency and Relative Difference

So far the relative difference calculated by the average number of PEs has been tanken into account. This study confirms that γ-hadron separation by looking at the signal measured in the upper and the lower layer is possible. To get a better feeling, 2D histograms for gamma and hadron induced showers for different energy ranges were produced. For this study again the column layout in combination with 500,000 gamma and proton showers, which were thrown at the center of the array are used. The utilized tank design is displayed in table 4.1.

The histograms shown in figure 4.3 and 4.4 are filled with the relative difference $\frac{N_{\mathrm{up}}-N_{\mathrm{down}}}{N_{\mathrm{down}}}$ separately calculated for each tank and air shower.

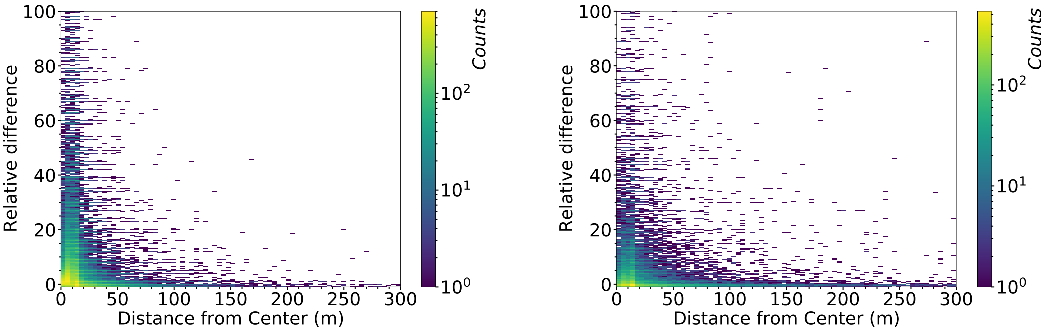

(a) (b)

Figure 4.3: 2D histograms for the energy bin $1 < E < 5$ TeV, displaying the relative difference dependency on the distance from the center of the shower core. The color bar indicates the number of relative differences detected dependent on the relative difference value and the distance. Histogram (a) is for gamma induced showers, while (b) is for proton showers.

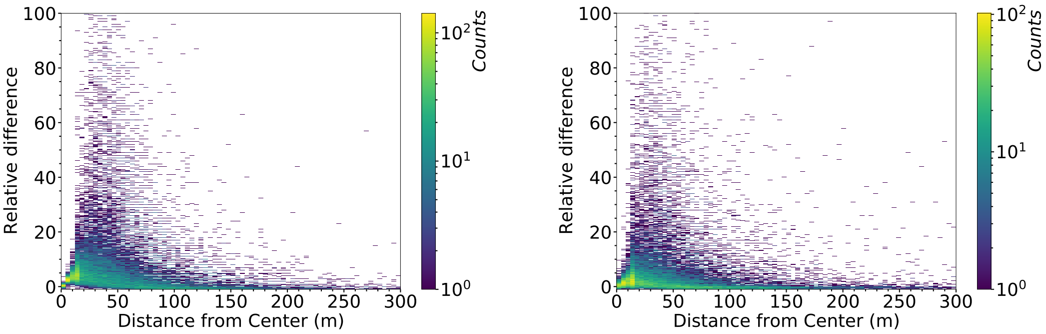

(a) (b)

Figure 4.4: 2D histograms for the energy bin $30 < E < 100$ TeV, displaying the relative difference dependency on the distance from the center of the shower core. The color bar indicates the number of relative differences detected dependent on the relative difference value and the distance. Histogram (a) is for gamma induced showers, while (b) is for proton showers.

Using this relative difference means that N_{down} must not be 0. Hence only tanks with $N_{\mathrm{PE}} > 0$ in both layers are used to fill the histograms. In figure 4.3 the 2D histograms for gamma (a) and a proton shower (b) are illustrated for an energy range of 1 to 5 TeV. If the two histograms are compared, it can be noticed that there are two major regions on has to be looked at.

- **Region near to the core:** For gamma showers a long tail up to high relative differences is visible. For proton showers this tail is much shorter.

- **Region for high relative differences and far away from the core:** While for gamma induced showers there is nearly no signal, for proton induced showers there are a few entries in the histogram due to muons.

The same observations can be made for higher and lower energies as well. In figure 4.4 the histograms are shown for the energy bin $30 < E < 100$ TeV. It can be seen, that the long tail for both gamma and hadron showers is shifted to the right. This behavior can be explained by the Molière-radius. It describes the lateral expansion of air showers that increases with increasing energy. Within this thesis only the region near to the core is taken into account and will be optimized. To clarify the need of a distance cut as well as an energy dependency of the γ-hadron separator, the studies on the 2D histograms were used to produce plots showing the average relative difference per distance (see figure 4.5). In both plots it can be seen that the average relative difference per distance at first is higher for gamma showers compared to proton showers. With increasing distance this behavior flips. Hence, to improve the separation power of the γ-hadron separator one should only use tanks for relative difference calculation up to a certain distance. The distance cut for showers with an energy between 1 and 5 TeV is at about 30 m. For the energy bin $30 < E < 100$ TeV this distance cut should be 100 m.

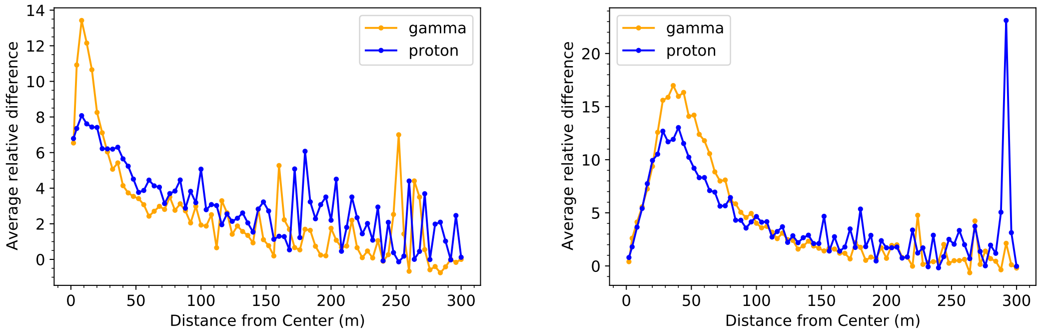

(a)

(b)

Figure 4.5: The average relative difference per distance, on the left (a) for the energy bin $1 < E < 5$ TeV, on the right (b) for the energy bin $30 < E < 100$ TeV

In summery, first, a distance cut is necessary to improve the separation power of the γ-hadron separator. Secondly, due to the energy dependency of the distance cut, an energy bin dependent γ-hadron separator is needed to ensure a well separation effectiveness.

4.2 γ-Hadron Separation with the Reference Design

For the further studies on γ-hadron separation the reference design is used. As in chapter 2.3 introduced and in figure 2.5 illustrated, the reference design consists of 6602 DLWCDc which were spread over an area of 301907 m^2. This design is adequate for more realistic studies, compared to the previously used column layout. Furthermore it brings up the possibility to compare the here developed γ-hadron separator with other separation methods. In the following the principles of the separation method as well as zenith and tank hit binning are introduced and are described in more detail.

Simulations

These studies on γ-hadron separation with the reference design were done with a total of one million simulated CORSIKA air showers. One half of them were thrown over an area of a circle with a radius of 1 km, while the other half had its impact point within the area covered by the reference design. In both cases the showers were $\frac{1}{r}$ distributed over the area. Which implies that most of the showers have their center of the shower front within the inner denser part of the array. The energy spectrum of the primary particles, follows again a power law with a spectral index $\Gamma = 2$. The energy spectrum starts at 31.6 GeV and ends at 1 PeV. The zenith angle of the EAS is not zero anymore, instead the angle is distributed over a range from 0° to 65°. The detector array simulated with HAWCsim is placed on an altitude of 4700 m.

Relative difference

As already motivated in section 4.1.1 the difference in the N_{PE} detected in the upper N_{up} and the lower layer N_{down} of the DLWCDc can be used to distinguish between gamma and hadron induced EASs. With the use of the reference design the question is asked whether to use the relative difference $\frac{N_{\text{up}}-N_{\text{down}}}{N_{\text{down}}}$ or $\frac{N_{\text{down}}-N_{\text{up}}}{N_{\text{up}}}$. Utilizing the relative difference $\frac{N_{\text{down}}-N_{\text{up}}}{N_{\text{up}}}$ would bring up many advantages in case of a realistic layout. First, the condition that there has to be signal in both layers is not further in demand. To avoid a division by 0, only the number of PEs detected with the upper layers PMT has to be higher than 0. Hence, more tanks with signal and therefore more relative differences can be used for identification of the shower. Secondly, according to this the definition of a tank hit becomes more naturally, what is shown below in the subitem about the tank hit binning.

Tank Hit Binning

All studies have been done up till now based on a binning in energy. In case of a γ-hadron separator binning in energy is not adequate, because energy is not an observable and there are still works in progress to develop energy estimators for SWGO. Instead in further studies on γ-hadron separation a tank hit binning is utilized. For this, information of the number of PEs detected in the upper layers of each DLWCDc unit of the reference design is used. A tank is considered to have been hit when $N_{up} > 0$. The sum of all tanks with $N_{up} > 0$ then results in the number of tank hits of the shower. This number increases with increasing size of the EAS, which depends on the energy of the primary particle of the shower. Of course this is only valid when the center of the shower front is within the area of the particle detector array, which is valid for the used simulated air showers. For the binning in tank hits the total number of tanks of the reference design is divided in ten bins which increase incrementally in size by 10%. The goal of this continual magnification in size is meant to ensure more statistics in the higher tank hit bins. The bins 0 to 9 are illustrated in table 4.2. For this thesis the tank hit binning as it is introduced turned out to be a good choice, nevertheless it has to be optimized. In figure 4.6 the correlation between tank hit binning and energy is displayed.

Bin	From	To
0	0	414
1	415	869
2	870	1370
3	1371	1922
4	1923	2528
5	2529	3195
6	3196	3929
7	3930	4736
8	4737	5624
9	5625	6601

Table 4.2: Tank hit binning for the reference design. The ten bins increase incrementally in size by 10%.

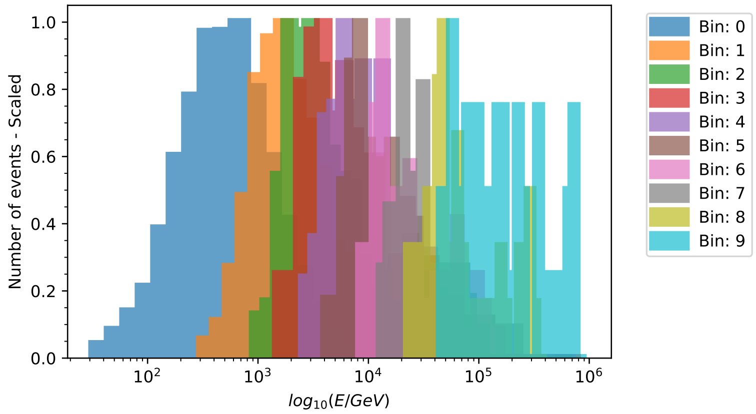

Figure 4.6: Correlation between tank hit binning and energy for γ-ray induced showers thrown on the reference design. The tank hit binning is displayed in table 4.2.

Zenith Binning

To ensure a satisfactory separation effectiveness in a realistic context, possible influences of different zenith angles have to be considered. Therefore air shower simulations with angles between 0° and 65° were used. The total range of 65° was split up into five bins. The size of the bins is equally distributed in $cos(\theta)$. In table 4.3 all five zenith bins are pointed out. To verify the need of a zenith binning, plots without zenith binning were made. Showers with a zenith angle between 0° and 45° were used for this studies. This range is represented by the assembly of zenith angle bins 0, 1 and 2.

Bin	From	To
0	0°	25°
1	25°	36°
2	36°	45°
3	45°	52°
4	52°	58°
5	58°	65°

Table 4.3: Zenith angle binning for the reference design. The size of the bins is equally distributed in $cos(\theta)$.

4.2.1 Average Difference per Event

The relative difference as well as a tank hit, a zenith angle binning and the simulations have been introduced up to now. Here, the relative difference $\frac{N_{\text{down}}-N_{\text{up}}}{N_{\text{up}}}$ of each tank of a shower event is taken up and is used for the introduction of a value for shower identification, later called difference cut. For the determination of this value the average relative difference or short average difference

$$\text{Average Relative Difference} = \frac{\sum_{N_{\text{Hits}}} \frac{N_{\text{down}}-N_{\text{up}}}{N_{\text{up}}}}{N_{\text{Hits}}} \tag{8}$$

is used. The number of tank hits in this formula is defined in equation 9 and represents the number of tanks with $N_{\text{up}} > 0$ which are contained in a circle with radius R_{cut}.

$$N_{\text{Hits}} = \sum_{i=0}^{6601} u(N_{\text{up},i}) \cdot w(r_i) \quad \text{with:} \tag{9}$$

$$u(x) = \begin{cases} 1: & x > 0 \\ 0: & x \leq 0 \end{cases} \quad \text{and} \quad w(x) = \begin{cases} 1: & x < R_{\text{cut}} \\ 0: & x \geq R_{\text{cut}} \end{cases}$$

Here $N_{\text{up},i}$ is the number of PE detected with the upper cells PMT of the tank i and r_i is the distance between tank i and the center of the shower front. The distance cut R_{cut} was motivated in section 4.1.2 and is set for the introduction of the separation method to 100 m. Later in section 4.2.4, R_{cut} will be optimized.

Calculating the average relative difference for each shower separately for all 2,000,000 showers results in distributions of the average relative differences. In figure 4.7 a distribution in form of a histogram is shown for tank hit bin 5 and zenith angle bin 0. Even though there is an overlap of the distributions, most gamma events have lower average relative differences than proton induced showers. The difference cut is now a value of the average relative difference on the x-axis where one can decide wether the primary particle is a γ-ray or a proton. In case of this example histogram one would naively choose -0.72 as a value for the difference cut. So any average relative difference of a shower which is on the left side of the cut would be identified as a γ-ray induced events, while all event right of the cut are classified as proton showers. Due to the overlap no perfect separation is possible, which means there is always a fraction of events which are wrongly identified. Hence it is desirable to reduce this number of events, by finding the best difference cut value. For this optimization ROC-curves as well as the signal-to-noise ratio (SNR) are used, which are both introduced in the following sections. Afterwards, when one is able to clarify the separation effectiveness an optimization on the distance cut R_{cut} is done.

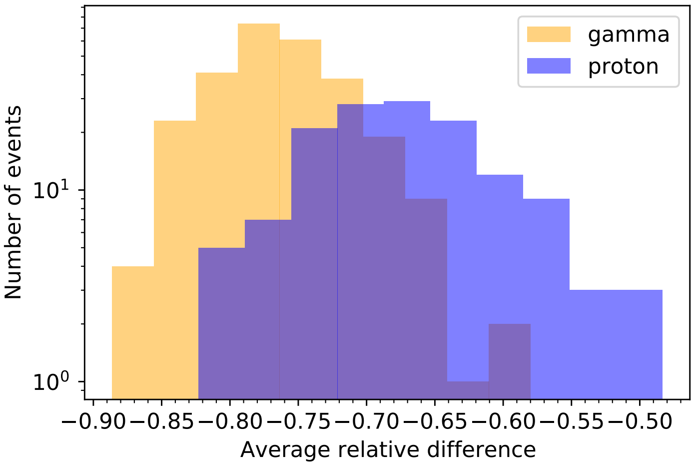

Figure 4.7: Distribution of the average relative difference for gamma and proton induced air showers. The histogram represents showers with zenith bin 0 and tank hit bin 5. For the calculation of the average relative difference, tanks within a maximal distance of 100 m from the center of the shower front are used.

4.2.2 ROC-Curve

A receiver operating characteristic (ROC)-Curve is a graphical plot used to show the diagnostic ability of binary classifiers. It was first used in signal detection theory but now it is applied for many other areas such as medicine, radiology, natural hazards and machine learning. In this section it will be shown how a ROC-Curve is created and how to interpret the ROC curve. For additional information see (Kustra & Telea 2019) and (Hajian-Tilaki 2013).

Creating a ROC-Curve:
A discrete classifier that only returns the predicted class gives a single point on the ROC space. But for probabilistic classifiers, which give a probability or score that reflects the degree to which an instance belongs to one class rather than another, a curve can be created by varying the threshold for the score. This is indicated in figure 4.8 for two average relative difference distributions for gamma and hadron induced air showers.

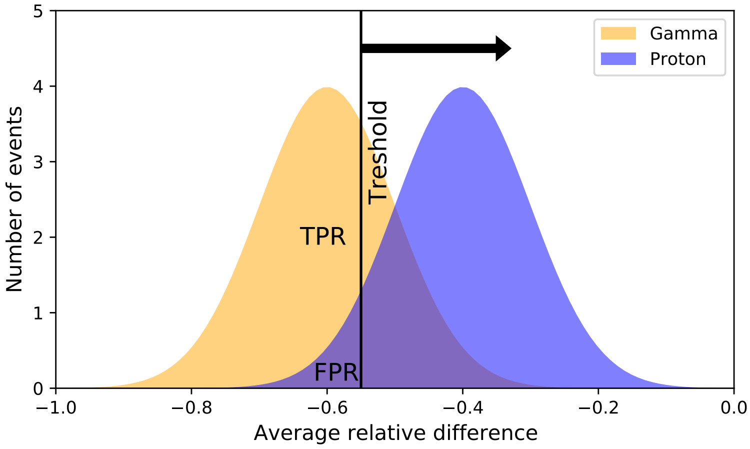

Figure 4.8: Sketch of two gaussian distributions, displaying the distribution of the average difference per shower for gamma and proton showers. The threshold, is indicating the cut which will be used for γ-hadron separation. True positive is the area designated as "Gamma" on the left side of the threshold. False positive denotes the area named "Proton", which is on the left of the threshold.

The curves of both classes are in this case produced by gaussian distributions with different mean values. True positive is the area designated as "Gamma" on the left side of the threshold. False positive denotes the area named "Proton", which is on the left of the threshold. Total positive is the total area under the "Gamma" curve while total negative is the total area under the "Proton" curve. Equation 10 displays the true positive rate, while equation 11 shows the false positive rate. By calculating the true positive rate (TPR) and false positive rate (FPR) at different threshold values and plotting them against each other a ROC-Curve is created.

$$TPR = \frac{\text{True Positive}}{\text{Total Positive}} = \frac{\text{Number of } \gamma\text{-ray showers}}{\text{Total Number of } \gamma\text{-ray showers}} \tag{10}$$

$$FPR = \frac{\text{Fals Positive}}{\text{Total Negative}} = \frac{\text{Number of proton showers indentivied as a } \gamma\text{-ray shower}}{\text{Total Number of proton showers}} \tag{11}$$

Interpreting a ROC-Curve:
ROC is a plot of signal (True Positive Rate) against noise (False Positive Rate). The model performance is determined by looking at the area under the ROC curve. For a better understanding of the performance of the γ-hadron separator

and for interpretation of the ROC-Curve in figure 4.9, several distributions with varying mean values of the average difference for gamma and hadron induced showers are illustrated with associated ROC-Curves.

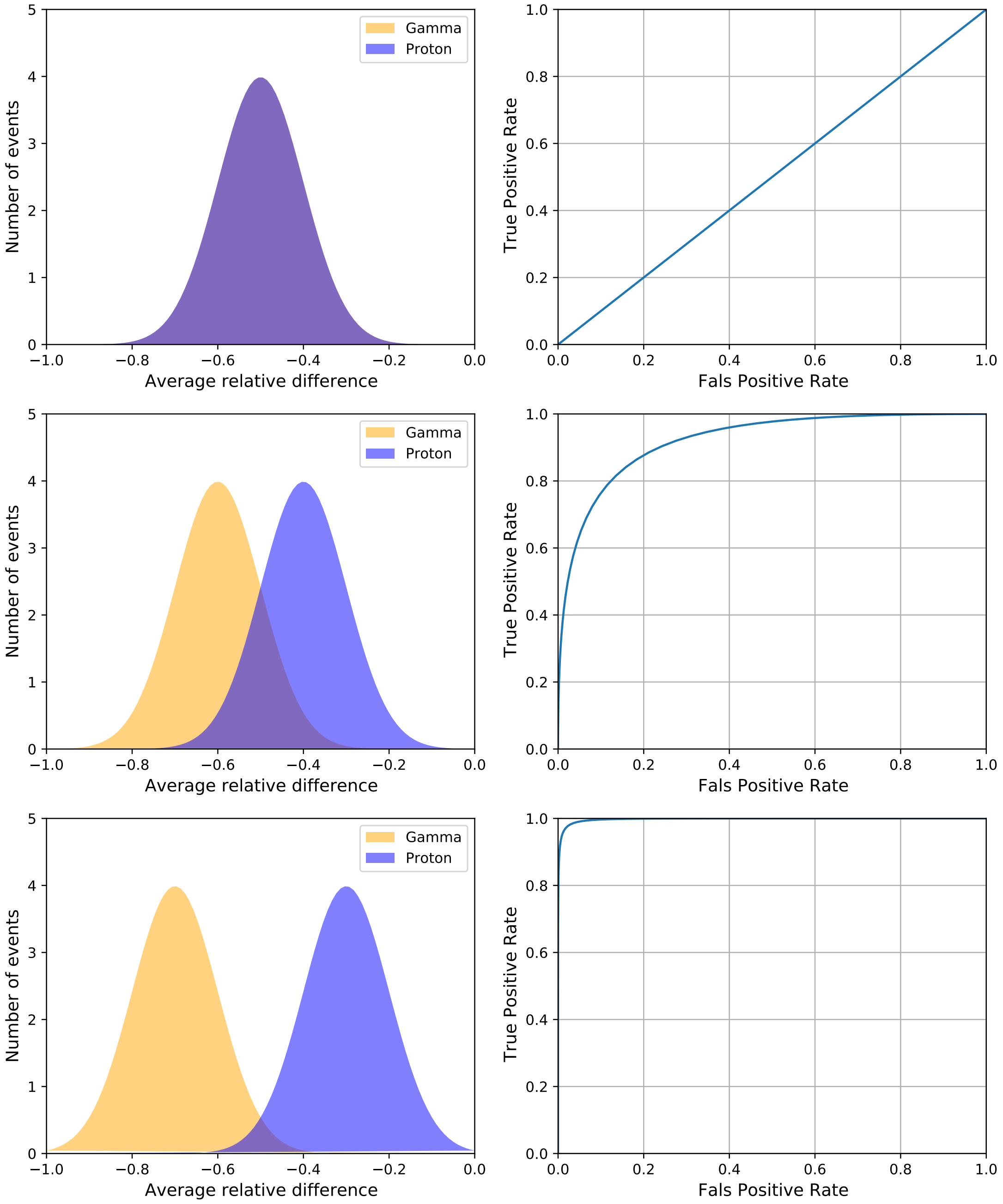

Figure 4.9: Three examples, which indicate how the ROC-Curve looks like when the class separation (i.e. the model performance) improves.

In the first row distributions for the average relative difference of gamma and proton showers are exactly overlying (see histogram on the left). On the right, the ROC-Curve is plotted. It can be seen that the curve in this case is described by the angle bisector. This can be interpreted as guessing. On the left hand side of the second row the the mean values of the gaussian distributions are -0.6 and

-0.4, which results in visible better separation between the two classes. On the right hand side the ROC-Curve confirms this observation, which means that the area under the curve increases. In the third and last row a very good separation is displayed between the two classes. In the histogram on the left there is only a small overlap and therefore almost a perfect separation. This results in a ROC-Curve with a nearly maximal area under the curve. The best possible performance is achieved for a TPR of 1 and a FPR of 0. In this case the area under the curve is maximal, which means the distributions of both have no overlap. In the following chapters ROC-Curves in combination with the SNR are used for the optimization of the γ-hadron separation.

4.2.3 Signal-to-Noise Ratio Optimization

In the end of section 4.2.1 it is described how histograms are produced, as shown in figure 4.7. This histograms for each tank hit and zenith bin separately can than be used to create ROC-curves as shown in chapter 4.2.2. To start with the search of the best difference cut value of a histogram, both the histogram as well as the according ROC-curves have to be produced. But before finding this value the best difference cut value has to be defined. In the case of hadron rejection most frequently used parameter for this is the SNR which is defined in equation 12.

$$\mathrm{SNR} = \frac{\int \mathrm{Signal}}{\sqrt{\int \mathrm{Background}}} = \frac{\mathrm{TPR}}{\sqrt{\mathrm{FPR}}} \tag{12}$$

Here the TPR as well as the FPR is the information which is plotted in the ROC-curve. In terms of γ-hadron rejection the TPR is the probability to identify a gamma, also called gamma efficiently and the FPR represents the probability to wrongly identify a proton as a gamma, also called hadron rejection. As defined above the SNR can only adopt positive values between zero and infinity, which is the case for FPR=0. In figure 4.10 an example histogram and ROC-curve calculated for this is shown. As seen in the ROC-curve the condition FPR=0 and therefore the highest SNR is only reached for low probabilities to identify a γ-ray shower, which means one would throw away a lot of showers. For clarification, this would be the case for a distance cut below ~ -0.83 in the histogram right to the ROC-curve. To avoid this behavior the minimal gamma efficacy which has to be achieved through optimization is set to 0.7, displayed through the dashed blue line in part (b) of figure 4.10. Now in order to find the best difference cut value, SNR of all points of the ROC-curve with a probability to identify a gamma higher than 0.7, are calculated and compared in the example indicated through the blue dashed line. At the blue line the SNR is 1.813 and if there would not be a point with a higher SNR above this threshold, the difference cut would be represented by this blue point. But as highlighted with the green dot a point with a gamma efficacy of 0.72 and a higher SNR on the curve is found. This green dot represents now the difference cut with the best separation power. To receive the value of the difference cut one has to look back into the definition and creation process of ROC-curves (chapter 4.2.2), where it is said that each point on the curve stands for a specific threshold. The threshold and therefore also the difference cut in case of the green labeled point is -0.739 and is pointed out through a green dashed vertical line in the histogram next to the ROC-curve. The hadron rejection in this case is 0.15. With this method, for a generalized distance cut of 100 m the best difference cut is found. In the next step it is tried to combine this with an optimization of the distance cut to increase the SNR even more.

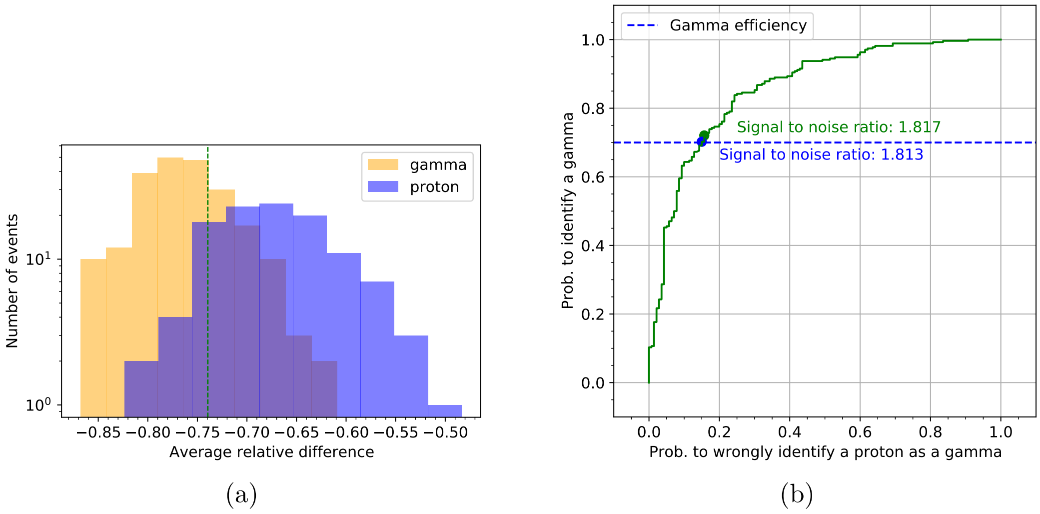

(a)

(b)

Figure 4.10: (a): Distribution of the average relative difference for gamma and and proton induced air showers. The histogram represents showers with zenith bin 0 and tank hit bin 5. Tanks within a maximal distance of 100 m from the center of the shower front are used. In (b), the according ROC-curve is shown with SNR at 0.7 gamma efficiency (blue) and best SNR (green).

4.2.4 Distance Cut Optimization

As presented in section 4.1.2, the distance between a given tank and the center of the shower core plays a crucial role in the value of the relative difference of the tanks. It seems to be the case that the gap between the relative difference of gamma and hadron induced air showers not only varies with distance but also becomes zero and then changes sign for tanks farther away from the impact point. Hence the idea is to only factor tanks within a certain range in order to optimize the average of the relative difference. In order to optimize the distance cut, histograms for all binnings were made for 60 different distance cut values. The 60 distance cuts range from 5 to 300 m, with steps of 5 m. For the introduction of the method, only the optimization for showers obtained in tank hit bin 5 and zenith angle bin 0 is shown.
First step in this process is to produce ROC-curves for each distance cut as shown in figure 4.11 (a). After this the best point on the ROC-curve is searched for each distance cut and therefore for each curve separately. This procedure is described in chapter 4.2.3 for distance cut 100 m.

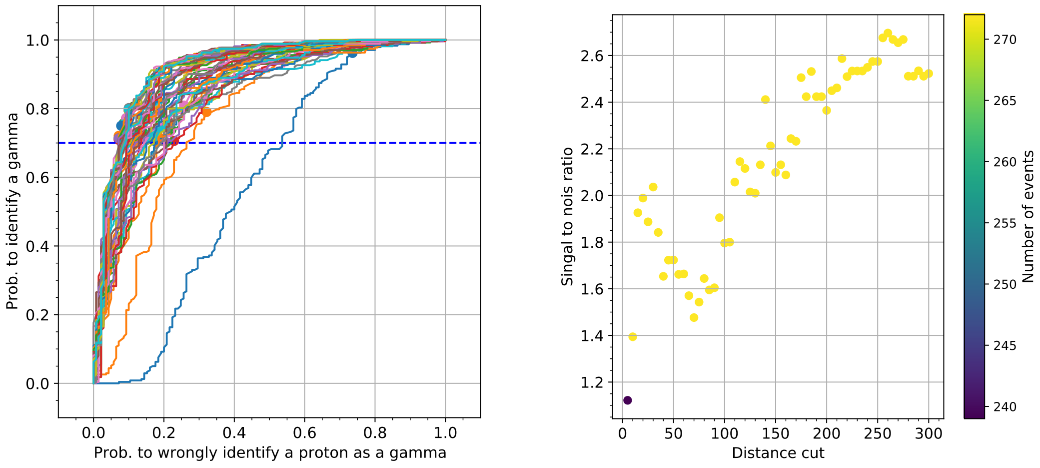

(a) (b)

Figure 4.11: (a): ROC-curves for zenith bin 0 and tank hit bin 5 for 60 different distance cuts. (b): SNR of each best point of the ROC-curve over the distance cut. The maximum of the SNR is achieved for a distance cut of 260 m.

The next step in the optimization is to plot the SNR of each best point of the ROC-curve over the distance cut (see 4.11 (b)). As can be seen in the plot, the SNR at first increases for increasing distance cut and then decreases after a maximal SNR. Due to the aim of optimization of the SNR, the maximum found then represents the best distance cut for γ-hadron separation and simultaneously brings up the difference cut.

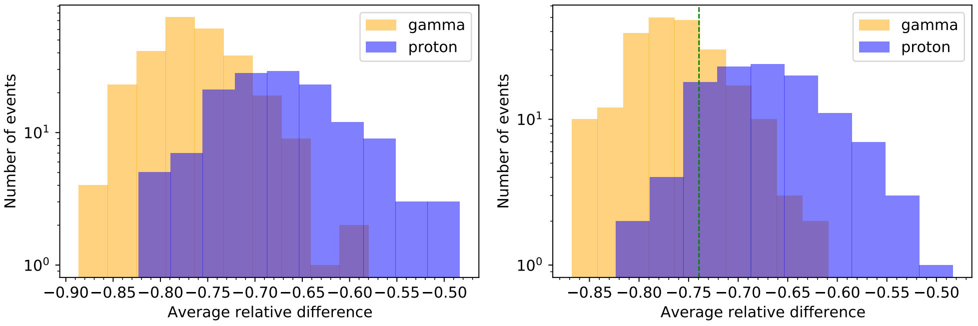

(a) (b)

Figure 4.12: (a): Histogram for 100 m distance cut, zenith bin 0 and tank hit bin 5. (b): Histogram with optimized distance cut of 260 m.

In the here shown example the optimized distance cut is 260 m. The ROC-curve and especially the best point of this curve result in a difference cut of −0.742. To clarify the influence of the distance cut on the separation power, in figure 4.12 histograms for 100 m distance cut (left) and optimized distance cut of 260 m (right) are illustrated. It is easily visible that the optimization process has worked well. The peaks of the right histogram are much better separated and the overlap is smaller. Even if a clear maximum was found in figure 4.11 (b), this does not always have to be the case. Especially for high tank hit bins it often happens that there are several maximums. In such cases, the point with the best SNR in addition to the highest gamma efficiency is chosen (see figure A.3 and A.4).

4.2.5 Separation Power of the Reference Design

In the last section, an explicit example (tank hit bin 5 and zenith angle bin 0) was used to describe the γ-hadron separation method and its optimizations. For the evaluation shown here, this method was applied on all the other tank hit bins and zenith angle bins as well. In figure 4.13 the fraction of events which pass the γ-hadron cut are plotted vs the tank hit binning for different zenith bins.

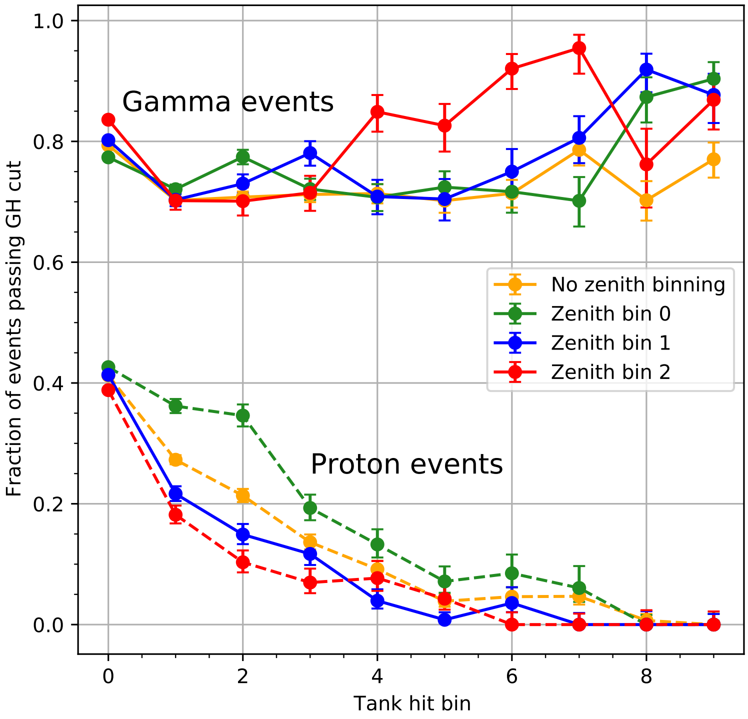

Figure 4.13: γ-ray efficiency and hadron rejection power as a function of tank hit bins after optimization of the difference and distance cuts for different zenith angles.

To verify the need of a zenith binning, additional studies without zenith binning are made, which are displayed in orange. For this studies showers with a zenith angle between 0° and 45° are used, which represents the combination of zenith bin zero, one and two. As can be seen, the fraction of gamma events which pass the cut is above 0.7 for all shown zenith angles. This is the case due to the definition of the γ-hadron separators minimal gamma efficiency. Going to higher tank hit bins results in an increase of the fraction of gamma events passing the cut. In case of proton events this behavior is the other way around. For tank hit bin zero about 40% to 45% events pass the γ-hadron separator. This percentage decreases below 10% for all zenith bins within tank hit bin seven. As the fraction of protons passing the separator is exactly zero for tank hit bin nine, a nearly

perfect separation occurs. This is also the case for tank hit bin six, seven and eight in combination with zenith bin two. Of course this does not represent the reality and can be justified by less statistics within this bins. Furthermore, it can be seen that the gap between the fraction of proton events and gamma events, which pass the γ-hadron cut, increase with increasing zenith bins. Although that happens, the difference is not particularly great and in most cases the fraction without zenith binning is in between the fraction for zenith bin zero and zenith bin two. Based on these results, it can be justified that no division into zenith bins is necessary to improve the separation power.
In order to compare whether it matters where the showers hit the array, further investigations were made. Therefore the γ-hadron separator is applied to showers which hit the inner and the outer array separately. For this purpose, the entire optimization process was run for both areas. The results are displayed in figure 4.14. Here the γ-ray efficiency and hadron rejection power are plotted for tank hit bin zero.

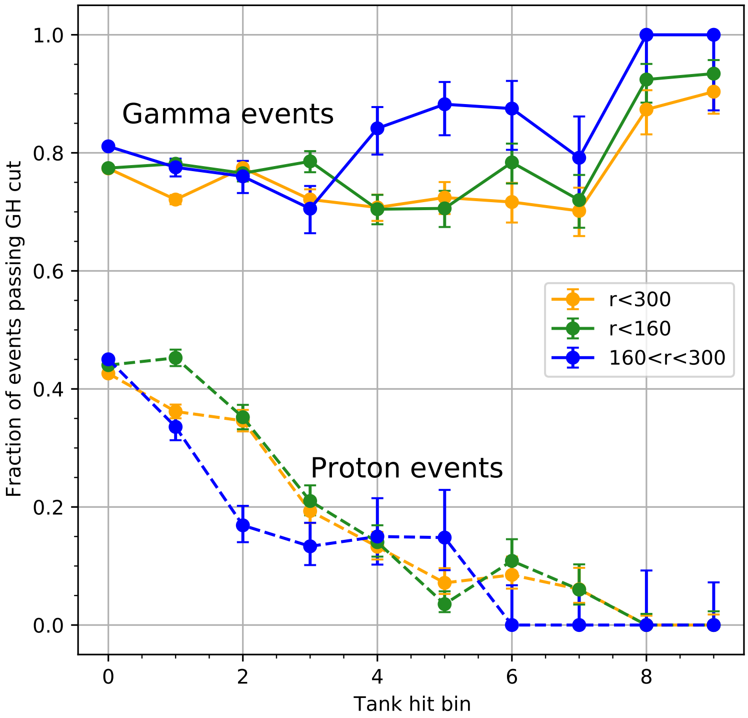

Figure 4.14: γ-ray efficiency and hadron rejection power as a function of tank hit bins after optimization of the difference and distance cuts. The colors indicate different impact point areas. Orange indicates all showers with center of the shower core within a 300 m radius from the center of the array. Blue and red illustrate γ-ray efficiency and hadron rejection power for showers landing within the inner and outer array.

In order to compare the results, additionally the fraction of events which land within the whole array and pass the γ-hadron cut is plotted. In case of gamma showers, applying the cut separately on the two parts of the array could help to increase the gamma efficiency. Especially for tank hit bins higher than three the achieved gamma efficiency in the inner array and in the outer array is higher compered to that which comes up using the entire array. Nevertheless, the gamma efficiency achieved in the outer array for high tank hit bins must be viewed critically, especially since the hadron rejection power is zero for these tank hit bins. This can be explained by gamma and proton histograms that are perfectly separated from each other, which indicate too few statistics. The low statistics can be explained by the energy and space distribution of the primary particles mentioned in simulations part chapter 4.2. The hadron rejection power achieved with the whole array and with the inner array is nearly the same. Only the fraction of protons landing in the outer array and pass the γ-hadron cut, is lower in most cases, which may be a conclusion of the low statistics. In summary, the differences in separation power are too small to justify a division of the γ-hadron separator into inner and outer array. This has the advantage that there is no need of several different cuts, which simplifies the gamma hadron separation method.

4.2.6 Effective Area

The effective area is part of the instrument response functions that is used to convert a number of detected counts into a physical flux. It is defined as

$$A_{eff} = \int_A \epsilon(\vec{r})dA \tag{13}$$

where the integrated area A is an arbitrary large area which extends well beyond the area of the detector. ϵ is the detection probability for an event with center of the shower front at point $\vec{r}$. It depends for example on the energy, the zenith angle, the type of primary particle and applied event cuts. Possible event cuts are restrictions on the zenith angle, a minimal threshold for triggered tanks as well as an applied γ-hadron separation. In this chapter the effective areas will be given as function of energy and particle after implementation of different acceptance cuts, once with and once without γ-hadron separation. The applied acceptance cuts are listed in table 4.4.

Event trigger condition:	more than 50 or 100 triggered tanks
Zenith angle cut:	zenith angle up to 45°
Core position cut:	Core position inside the detector boundaries

Table 4.4: Acceptance cuts for effective area calculation

As the separation power of the γ-hadron separator hardly depends on the zenith angle (see figure 4.13), the separation without zenith angle binning is used for the calculation of the effective area. The integration region is defined by the region for which events were simulated. The used showers are a part of the previously at the beginning of chapter 4.2 introduced simulations and include only the $500,000$ gamma and proton showers which are distributed over an area with a radius of 1 km. Since the impact points are distributed by $\frac{1}{r}$, a weighting is applied to obtain an equal distribution over the circular area. Showers with distances of about 1 km from the center of the shower core are utterly rarely reconstructed to be inside the detector array, so that the effective area after acceptance cuts should therefore not be significantly influenced. The detection probability ϵ is calculated as:

$$\epsilon = \frac{N_{\text{det}}}{N_{\text{MC}}} \tag{14}$$

with N_{det} the number of detected events that survive the respective cuts and N_{MC} the number of simulated events. As N_{det} is alway smaller than or equal to N_{MC}, ϵ can only assume values between zero and one. Figure 4.15 shows the effective areas after acceptance cuts versus the true simulated energy. First, results for the zenith angle cut and the event trigger condition ($>$ 100 tanks triggered) with γ-hadron separation are displayed. Secondly results without γ-hadron separation are presented. In order to investigate the influence of the γ-hadron separator on the effective area, the curve of effective area with a core position cut and an event trigger condition $>$ 100 tanks triggered is added to the plot as well. No point source simulations were available at the time this study was made.

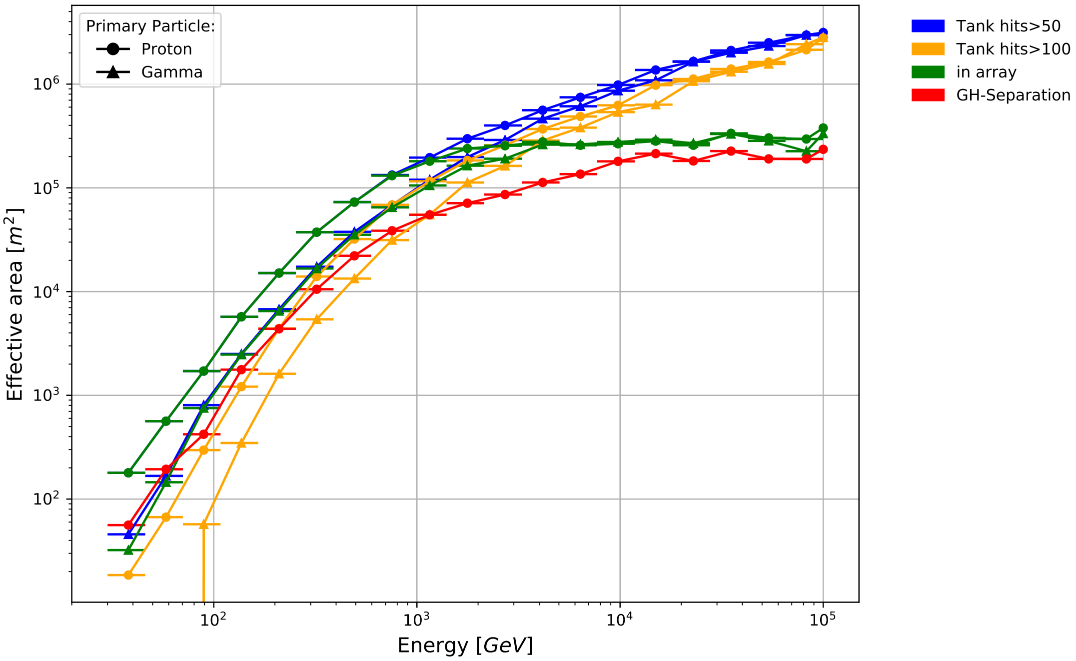

Figure 4.15: Effective area as a function of energy of the primary particle (gamma ray or proton) after applying the zenith angle cut and the event trigger condition, once with and once without γ-hadron separation. Additionally, as a preliminary stage for results with γ-hadron separation, the effective area with core position cut is shown.

Furthermore the spectral index Γ of the used simulated showers is -2, which in reality for hadrons would be roughly -2.7. Because of this no realistic studies on the background can be made and no curve for proton showers with applied γ-hadron separation is shown. On can learn from the plot that the choice of the event trigger condition has almost no influence on the effective area at higher energies. The use of the trigger condition ($>$ 50 tanks) instead of ($>$ 100 tanks) for energies below 1 TeV would lead to an increase in the effective area, by one order of magnitudes. As wanted for high energetic gamma induced showers, the effective area with applied γ-hadron separation hardly differs from the effective area with the core position cut. For energies below 1 TeV the difference increases with decreasing energy. This was expected due to the fact that the γ-ray efficiency of the γ-hadron separation method, becomes higher when going to higher tank hit bins (see figure 4.13). More influence on the effective area for both gamma and proton showers has the core position cut. Adding the core position cut to the already applied event trigger condition, leads to a decrease of the effective area's upper limit by a factor of 10. The highest effective area for gamma and proton showers with the core position cut represents nearly the detector area of the reference design. In general, more realistic point source and background simulations, e.g. of the Crab nebula, are necessary to correctly evaluate the effective area after the application of the γ-hadron separator, presented in this chapter.

4.3 Conclusion

Within this part of the thesis a basic γ-hadron separation method is introduced. Which uses the number of PEs detected in each tanks upper and lower layers PMT. At the beginning, the separator is motivated, based on previous column array layout studies on the relative difference between the $< N_{\mathrm{PE}} >$ detected in the upper layer with respect to the lower layer. This knowledge forms the basis for the further studies, which were made with the reference design. The reference design was particularly suitable for this purpose, as it has a realistic array of detector units and is widely used in the SWGO community. This has the advantage that the γ-hadron separation method can be easily compared with others and can be combined with them to improve the separation power even more. In combination with the reference design a possibility of the distinction of air showers was shown, which was optimized afterwards with the distance cut.
At the end of this chapter, the separation power is shown for the reference design for different zenith angles and areas of the reference design array. Due to these investigations, it can be concluded that the separation power has neither a dependence on the zenith angle nor on the position where the shower lands within the array. In addition to these advantages, there are others, such as the fact that it is a mighty simple method, for which no complicated algorithms are necessary. However, probably most importantly, it already runs for the reference design, can be easily applied to other array layouts and is complementary to other γ-hadron rejection parameters.

5 Summary and Outlook

In this thesis, SWGO's DLWCDc unit is investigated, to improve the performance of the Southern Wide-field Gamma-ray Observatory (SWGO). The next-generation γ-ray observatory is planned to be built in South America. With its wide field of view and nearly 100% duty cycle it will provide an energy sensitivity from 100s of GeV to 100s of TeV, using an array of WCDs (see Chapter 2) (Schoorlemmer 2019). For the decision on the DLWCDc design, studies on the inner wall color and the tank dimensions are made. For this purpose, two different array layouts are introduced. The column layout is used for studies on the single tank trigger probability and on saturation using the average number of PEs. A more realistic layout is used to see whether enough tanks are triggered. Due to these investigations and some considerations about cost estimation, a possible tank design is presented at the end of chapter 3. This choice includes black wall linings in the upper layer and white wall linings in the lower layer. The tank radius should not be larger than 2 m to save costs. For the tanks in the inner array, 4 m high top layers are useful to avoid saturation. In the outer array, the tanks are further away from each other, which results in larger saturation distances, so that lower heights, e.g. 2 or 3 m, can be chosen for the upper cell. While doing these studies, the focus was on saturation and tank triggering, which means one wants to trigger as many detector units as possible while avoiding saturation. Even if this is utterly important for the reconstruction, in the future, a glance on timing has to be taken as well, which is essential for direction reconstruction.

Although the cylindrical WCD design as used in HAWC has proven to be a suitable choice for EAS particle detector arrays and therefore the DLWCDc should also prove to be good. As a further development, there are other detector unit designs. The choice of the array arrangement and the detector unit design depends very much on the location and the prevalent environment of site. For example, if there is a lake, it will be possible to install the entire detector array in it. Also the use of two layered detector units is still under discussion. However, if one opted for single layer tanks, it would be necessary to imploy additional PMTs for muon tagging. As it will probably take until the end of 2021 before a final site selection is made, further simulations and studies are necessary to compare the different detector units. However, with the help of this work a basis for the choice of the tank dimensions and the inner tank color could be laid, which can be applied to different unit designs, e.g. pond solution or single layer WCD.

In the second part of this thesis, a basic γ-hadron separation method for the reference design is presented. The reference design itself is introduced in chapter 2.3. After optimizing a distance cut and the value for the relative difference, the separation power is shown for different zenith angles and areas of the reference design array. As a conclusion, the separation performance hardly depends on the zenith angle and the position where the shower lands within the array, so that neither zenith binning nor a distinction between inner and outer array for the γ-hadron separator is necessary.

In summary, due to the knowledge gathered during this work it can be said that this γ-hadron separator is a mighty simple one, for which no complicated

algorithms are necessary. Due to the few restrictions and cuts that are required, this method can be easily applied to various array layouts and combined with other γ-hadron separation methods.
To note, another planned γ-hadron separator for SWGO is developed by Samridha Kunwar from the Max-Planck-Institut für Kernphysik (MPIK) in Heidelberg. This template based method is also developed for double layer detector units and will be optimized for the reference design in the near future. A part of this optimization includes a distance cut. However, this does not cut tanks far away like for the separator shown here, but conversely only takes up tanks further away from the center of the shower core in order to differentiate the air showers. This fact favors simultaneous use and gives hope that both will support each other. To see the real correlation between both γ-hadron separation methods, further studies have to be done.
At last, the effective area of the reference design was under investigation. The results for γ-ray induced air showers with applied γ-hadron separation, seem to be promising and realistic. The in the SWGO science case white paper shown predicted effective area was estimated by upscaling the results from HAWC using the crab nebula (see Abeysekara et al. 2017). To be able to verify the expectations from the white paper, realistic point source and background simulations have to be included in SWGO's simulation chain.
Furthermore, more simulations would be needed to obtain better statistics for high tank hit or energy bins. This will also help in the determination of the average relative difference cut within the optimization chain of the γ-hadron separator. As next step, which ought to be done in the near future, is the implementation of the γ-hadron separator in the SWGO software framework.

A Appendix

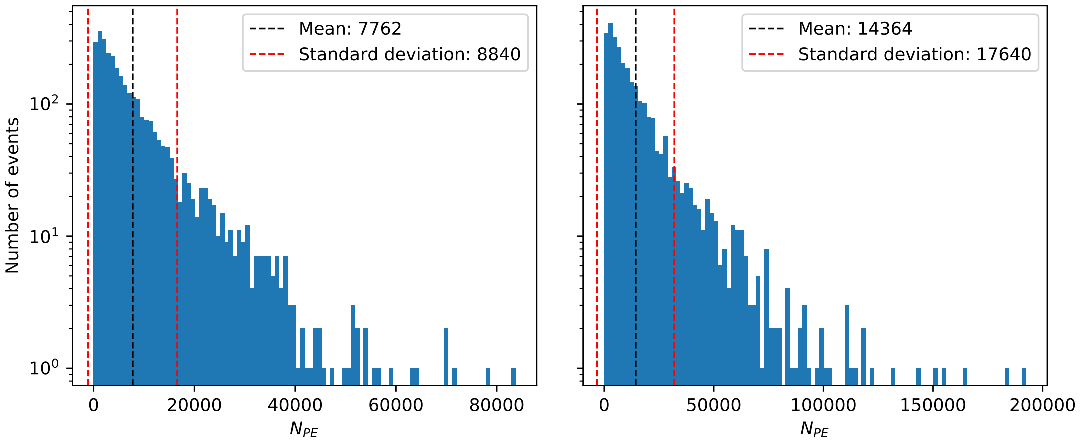

Figure A.1: The number of events dependent on the number of PEs (N_{PE}) for the energy bin $1 < E < 5$ TeV with black (left) and white (right) tank wall color configuration for the upper layer, for PMTs at a distance r of 2 m.

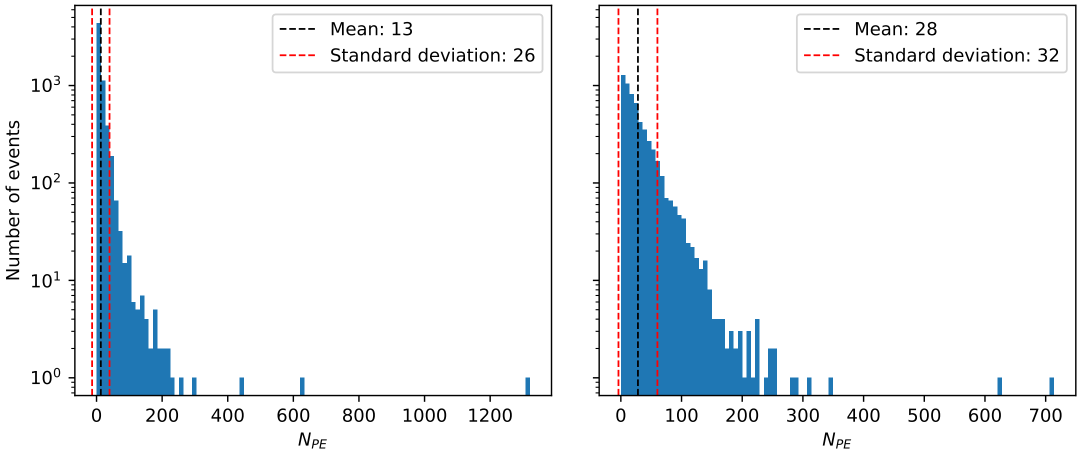

Figure A.2: The number of events dependent on the number of PEs (N_{PE}) for the energy bin $1 < E < 5$ TeV with black (left) and white (right) tank wall color configuration for the upper layer, for PMTs at a distance r of 40 m.

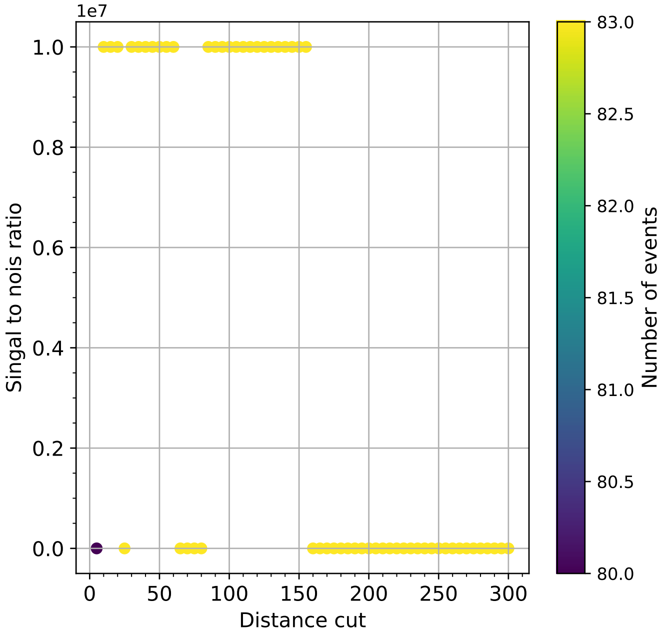

Figure A.3: SNR of each best point of the ROC-curve over the distance cut for zenith bin 0 and tank hit bin 9. Multiple maxima were found. At these maxima, the SNR is set to 10^7, which represents infinity. This is the case for a hadron rejection of 0.

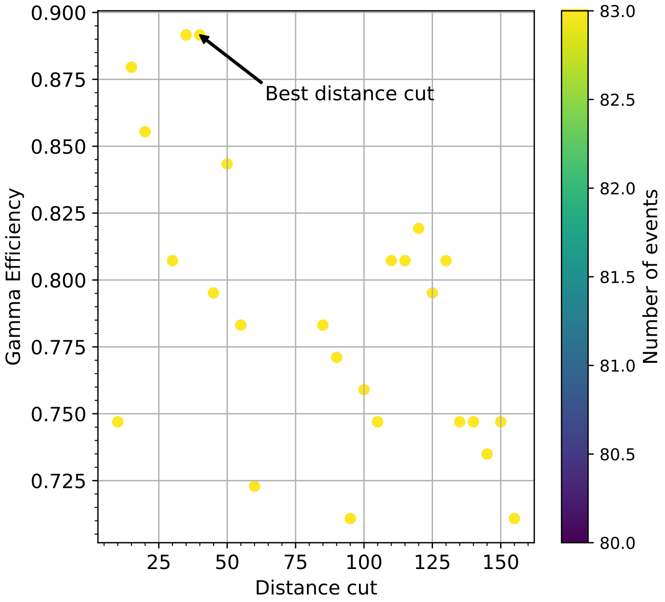

Figure A.4: Gamma efficiency of each found SNR maximum over the distance cut for zenith bin 0 and tank hit bin 9. The point with the best SNR in addition to the highest gamma efficiency has to be found. Hence, the distance cut value corresponding to the highest gamma efficiency in this plot is determined as the optimized distance cut. In the example shown here, the optimized distance cut is 40 m.

References

Abeysekara, A. U., Albert, A., Alfaro, R., et al. 2017, The Astrophysical Journal, 843, 39

Abreu, P., Albert, A., Alfaro, R., et al. 2019, The Southern Wide-Field Gamma-Ray Observatory (SWGO): A Next-Generation Ground-Based Survey Instrument for VHE Gamma-Ray Astronomy

Acharya, B. S., Agudo, I., Samarai, I. A., et al. 2018, Science with the Cherenkov Telescope Array

Agostinelli, S. et al. 2003, Nucl. Instrum. Meth. A, 506, 250

Aharonian, F. A., Akhperjanian, A. G., Barrio, J. A., et al. 2000, The Astrophysical Journal, 539, 317–324

Alaeian, H. 2014, An Introduction to Cherenkov Radiation, `http://large.stanford.edu/courses/2014/ph241/alaeian2/`

Assis, P., Barres de Almeida, U., Blanco, A., et al. 2018, Astroparticle Physics, 99, 34–42

Barrau, A. et al. 1998, Nucl. Instrum. Meth. A, 416, 278

Barres de Almeida, U. 2021, Astronomische Nachrichten, 342, 431–437

Blandford, R., Simeon, P., & Yuan, Y. 2014, Nuclear Physics B - Proceedings Supplements, 256-257, 9, cosmic Ray Origin – Beyond the Standard Models

Blasi, P. 2009, Physical Review Letters, 103, 051104

Blümer, J., Engel, R., & Hörandel, J. R. 2009, Progress in Particle and Nuclear Physics, 63, 293

Bothe, W. & Kolhörster, W. 1929, Zeitschrift für Physik, 56, 751–777

Bustamante, M., Carrillo Montoya, G., de Paula, W., et al. 2010, High-energy cosmic-ray acceleration

Cui, W. 2009, TeV Gamma Ray Astronomy, Research in Astronomy and Astrophysics 9 (2009) 841-860

Durham University. 2014, Ground Based Gamma Ray Astronomy, `https://www.dur.ac.uk/cfai/vhegammaraygroup/physics/groundbased/`

Fermi, E. 1949, Phys. Rev., 75, 1169

Fernandez, E. 2006, Nuclear Physics B - Proceedings Supplements, 151, 381, vERY HIGH ENERGY COSMIC RAY INTERACTIONS

Frank, I. M. & Tamm, I. E. 1937, Compt. Rend. Acad. Sci. URSS, 14, 109

Greisen, K. 1966, Phys. Rev. Lett., 16, 748

Hajian-Tilaki, K. 2013, Caspian journal of internal medicine, 4, 627—635

Hamamatsu Photonics K.K. 2007, Photomultiplier Tubes Basics and Applications, `https://www.hamamatsu.com/resources/pdf/etd/PMT_handbook_v3aE.pdf`

HAWC. 2011, HAWC, `https://www.hawc-observatory.org/observatory/tanks.php`

Heck, D., Knapp, J., Capdevielle, J. N., Schatz, G., & Thouw, T. 1998, CORSIKA: a Monte Carlo code to simulate extensive air showers.

Hess, V. F. 1912, Phys. Z., 13, 1084

Hinton, J. 2004, New Astronomy Reviews, 48, 331–337

Holder, J. et al. 2009, AIP Conf. Proc., 1085, 657

Kustra, J. & Telea, A. 2019, Visual Analytics for Classifier Construction and Evaluation for Medical Data, ed. S. Consoli, D. Reforgiato Recupero, & M. Petković (Cham: Springer International Publishing), 267–287

Longair, M. S. 1992, High Energy Astrophysics: Volume 1, Particles, Photons and Their Detection - (Cambridge: Cambridge University Press)

Raffaela Solveig Busse. 2017, Setup and commissioning of a test stand for detailed investigations of quantum efficiency characteristics of photomultiplier tubes, and initial studies for IceCube-Gen2, `https://www.uni-muenster.de/imperia/md/content/physik_kp/agkappes/abschlussarbeiten/masterarbeiten/1703-ma_rbusse.pdf`

S.-O. Flyckt, Carole Marmonier. 2002, Photomultiplier Tubes Principles and Applications, `http://www2.pv.infn.it/~debari/doc/Flyckt_Marmonier.pdf`

Schoorlemmer, H. 2019, A next-generation ground-based wide field-of-view gamma-ray observatory in the southern hemisphere

Schoorlemmer, H., López-Coto, R., & Hinton, J. 2017, Baseline Design for a Next Generation Wide-Field-of-View Very-High-Energy Gamma-Ray Observatory

Tanabashi, M., Hagiwara, K., Hikasa, K., et al. 2018, Phys. Rev. D, 98, 030001

Tinivella, M. 2016, A review of Cosmic-ray electrons and fermi-LAT

Wagner, R. M. 2006, PhD thesis, Munich, Tech. U.

Weekes, T., Cawley, M., & Fegan, D. 1989, Observation of TeV Gamma Rays from the Crab Nebula Using the Atmospheric Cerenkov Imaging Technique

Zatsepin, G. T. & Kuzmin, V. A. 1966, JETP Lett., 4, 78

Acronyms

C

CMB	cosmic microwave background
CORSIKA	**CO**smic **R**ay **SI**mulations for **KA**scade
CR	cosmic ray
CTA	Cherenkov-Telescope-Array

D

DLWCDc	cylindrical double layer water cherenkov detector

E

EAS	extensive air shower
EM	electromagnetic

F

FPR	false positive rate

G

GZK	Greisen-Zatsepin-Kuzmin

H

HAWC	High-Altitude Water Cherenkov Observatory

I

IACT	imaging atmospheric cherenkov telescope

L

LHAASO	Large High Altitude Air Shower Observatory

P

PE	photo-electron
PMT	photomultiplier tube

Q

QE	quantum efficiency

R

r	distance from the center of the shower core (impact distance)
ROC	receiver operating characteristic

S

SNR	signal-to-noise ratio
SWGO	Southern Wide-field Gamma-ray Observatory

T

TPR	true positive rate

V

VHE	very-high energy

W

WCD	water cherenkov detector

Acknowledgements

I would like to thank everyone who supported me during my master thesis. Special thanks to:

- Prof. Dr. Christopher van Eldik for giving me the opportunity to work on this interesting subject and for supervising my thesis.
- Vikas Joshi for the great support and for his valuable comments.
- The whole SWGO group for providing a pleasant working atmosphere.
- My friends supporting me through this difficult time.
- Alexander Vogel and Sven Kallert for their help, having an open ear and getting me through this time.
- Kai Neumann and Sebastian Konrad for plenty of academic discussions.
- My parents and grandparents for enabling my whole studies and for their patience and help.

Statement of Authorship

I hereby certify that this thesis has been composed by me and is based on my own work, unless stated otherwise. No other person's work has been used without due acknowledgement in this thesis. All references and verbatim extracts have been quoted, and all sources of information, including graphs and data sets, have been specifically acknowledged.

place, date	signature